

Hanging glacier avalanche (Raunthigad - Rishiganga) and Debris flow disaster of 7th February 2021, Uttarakhand, India, A Preliminary assessment

Renoj J Thayyen (✉ renojthayyen@gmail.com)

National Institute of Hydrology <https://orcid.org/0000-0002-9523-0313>

P.K Mishra

National Institute of Hydrology

Sanjay K. Jain

National Institute of Hydrology

John Mohd Wani

National Institute of Hydrology

Hemant Singh

National Institute of Hydrology

Mritunjay K. Singh

National Institute of Hydrology

Bankim Yadav

IIT Roorkee: Indian Institute of Technology Roorkee

Research Article

Keywords: Ice-rock avalanche, Debris flow, Rishiganga, Hanging Glacier, Disaster, Himalaya

Posted Date: March 23rd, 2021

DOI: <https://doi.org/10.21203/rs.3.rs-340429/v1>

License:  This work is licensed under a Creative Commons Attribution 4.0 International License.

[Read Full License](#)

1 **Hanging glacier avalanche (Raunthigad - Rishiganga) and Debris**
2 **flow disaster of 7th February 2021, Uttarakhand, India, A Preliminary**
3 **assessment**

4 Renoj J. Thayyen^{1*}, P.K Mishra¹, Sanjay K. Jain¹, John Mohd Wani¹, Hemant Singh¹,
5 Mritunjay K. Singh^{1,2} and Bankim Yadav³

6 ¹National Institute of Hydrology, WRS Division, Roorkee-247667

7 ²National Space Science and Technology Center (NSSTC), UAE University, P.O Box.
8 15551, UAE

9 ³Indian Institute of Technology Roorkee, Roorkee, 247669

10

11 * Correspondence: renojthayyen@gmail.com

12 **Abstract**

13 A catastrophic debris flow in the Rishiganga and Dhauri ganga river in Uttarakhand,
14 India on 7th February 2021 left a trail of disaster. Around 200 people lost their lives,
15 two hydro-power project were badly damaged and a bridge across the Rishiganga
16 River was washed off in the event. Study shows that the debris flow is caused due
17 detachment of 0.59 km² right lobe of a hanging glacier and resultant ice-rock
18 avalanche. This right lobe of the glacier was located over a mountain slope having an
19 average slope of 35° at 4700-5555 m a.s.l. and travelled 12.4 km before hitting the
20 infrastructure projects. Role of precipitation, snow cover, land surface temperature
21 and permafrost processes were investigated for identifying causes of the event. Since
22 2012, monsoon precipitation and mean annual land surface temperature (LST)
23 showed significant increasing trend. Snow cover during monsoon months showed
24 increasing trend and September, October and November experienced decreasing
25 trend at glacier elevations. Mean annual LST increased from -0.3 °C in 2012 to a peak
26 of 0.4 °C in 2016. Central lobe of the glacier advanced during this period and eventually
27 fell off in 2016 suggesting that the LST warming forced reduction of frictional drag at
28 the interface facilitating its advancement and eventual dislodgement. Permafrost
29 modelling suggest warm permafrost below 50 m and conditions favorable for intense
30 frost cracking at to 10-15 m. At ~40 m depth, the delayed response of 2012- 2016
31 warming produced peak positive temperature conditions by December and probably
32 facilitated the formation of thin film of water at the deeper layers acting as a lubricant

33 for glacier sliding. It is also suggested that the increase in summer precipitation might
34 have forced thickening of the accumulation area and thereby increasing the shear
35 stress for sliding of the glacier. It is proposed that the recent change in the weather
36 conditions in the region is primarily responsible for this event through geological,
37 glaciological and permafrost processes. Flood modeling study suggest a flood volume
38 of ~10 MCM generating 24.5 m flow depth at the bridge site with 12.7 m/s flow velocity.
39 The event highlighted the need for improved monitoring of the cryospheric areas of
40 the Himalaya to capture the early warning signs for better preparedness.

41

42 **Keywords:** Ice-rock avalanche, Debris flow, Rishiganga, Hanging Glacier, Disaster,
43 Himalaya

44

45 **1.0 Introduction**

46

47 A devastating flash flood occurred on Rishi Ganga and Dhauliganga river, which
48 initiated from the upper glacier region of Raunthi gad in the Chamoli district
49 Uttarakhand. The event happened on 7th February 2021 and had a devastating effect
50 downstream. Flood impact was mainly constrained to the infrastructure project along
51 the river reach starting from a 13.2 MW small hydropower project across Rishiganga
52 (2050m a.s.l.) and then dismantling a bridge across the Rishiganga (1985 m a.s.l.) at
53 the confluence of Dhauliganga. Further downstream at 4 km on Dhauliganga, the flood
54 destroyed the 520 MW Tapovan-Vishnugad hydropower project (1800 m a.s.l.). The
55 tunnel under construction for the Tapovan-Vishnugad project become the major
56 disaster site, more than 50 people lost lives and more than 150 people still missing.
57 Tapovan dam structure is filled with flood deposits highlighting the amount of debris
58 brought down by the event. This debris flow in the peak winter month of February
59 caused strong speculation about the cause of this event. Considering that heavy
60 snowfall occurred in the region a couple of days ahead, i.e. on 4th and 5th February
61 2021, therefore an avalanche trigger is suspected as the Rishiganga basin has around
62 52 glaciers with a 262 km² glacier area. Five of these glaciers have an area >50 km²
63 (Sangewar & Shukla, 2009) therefore, the possibility of a glacial lake outburst flood
64 (GLOF) is also considered. However, a recent glacial lake inventory of the region
65 prepared as part of an ongoing project under National Mission on Sustaining

66 Himalayan Ecosystem (NMSHE) sponsored by the Department of Science and
67 Technology, Govt. of India recorded 7 glacier lake in the area with none of them is
68 vulnerable as per standard criteria (Jain, 2021, Under preparation). The high-
69 resolution satellite images on the following day, 8th February (Source: Planet lab,
70 digital.hbs.edu/platform-rctom/submission/planet-labs-satellite-imagery-to-better-
71 humanity/) given the first insight on the location of the flood initiation point in the
72 Raunthigad catchment, a tributary of River Rishiganga. It has shown an avalanche site
73 on the northern slopes at an elevation of 4700-6000 m a.s.l. Subsequent analysis of
74 the previous day's images clearly showed that the avalanche occurred during the
75 intervening period of 6th and 7th. This is followed by the availability of photos taken
76 during aerial reconnaissance survey conducted by various agencies, which clearly
77 showed the source area of the avalanche (NTPC, personnel communication). By
78 tracing back, the site information on google earth images and other satellite images
79 showed that a "hanging glacier" was occupying the detachment area, which suggested
80 that the event was initiated as ice-rock avalanche. The right lobe of the hanging
81 glacier, which got detached, had a length of ~1.6 km and an average width of ~550 m
82 occupied the northern slope in the Raunthi gad catchment. This hanging glacier of
83 1.23 km² area situated at an elevation range of 4695-6000 m a.s.l. and detached right
84 lobe had an area 0.59 km². This ice-rock avalanche resulted in massive debris flow
85 with long-runout distance travelled through 14.35 km along Raunthigad to hit the
86 hydropower project barrage (HEP-1) and washed off the bridge across River
87 Rishiganga further downstream. About 7.4 km downstream, the debris flow devastated
88 the Tapoban barrage. As the event occurred at forenoon time around 11:00 AM, local
89 residents could capture several live images and videos of the event illustrating the
90 catastrophic dimensions of the floods (Fig. 1)



91

92 Figure 1: a) Pre-flood NTPC barrage (HEP 2) at Tapovan, b) Post flood photo showing
 93 severe damage to NTPC barrage at Tapovan C) Site of washed off bridge across
 94 Rishiganga upstream of NTPC barrage D) Site of Rishiganga (HEP-1) project site

95 *Photo courtesy: NTPC and BRO*

96

97 This is a very significant event not only in terms of the catastrophic disaster it caused
 98 along its flow path but also in terms of breaking of a large glacier mass which is a very
 99 rare phenomenon in the glaciated regions of the world and more so in the Himalayas.
 100 This event is followed by a previous catastrophic event in 2013 in the same region
 101 known as the “Kedarnath deluge”. The 2013 event was caused by a combination of
 102 factors, including extreme rainfall, sudden snowmelt under excessive rainfall and
 103 breaching of Chorabari lake (Dobhal et al., 2013; Dubey et al., 2013; Allen et al., 2016)
 104 indicate the serious challenges faced by the mountain community in a warming
 105 climate. Hence, understanding the causes leading to this event is of utmost importance
 106 for assessing the disaster potential of the region in particular and also for the entire
 107 Himalayan region. Glacial lake outburst flood (GLOF) is well appreciated as a potent
 108 disaster of glacial origin, and a couple of recent events increased its threat perception
 109 in the region (Komori et al., 2012, Raj et al., 2012, Schmidt et al., 2020, Thayyen, 2020).
 110 Cloudburst is another disaster that is increasingly becoming more regular in the
 111 Himalayan region (Das et al., 2006., Thayyen et al., 2013, Dimri et al., 2017, Kumar

112 et al., 2018). Snow avalanche is also identified as a major disaster in the region, and
113 forecasting and modelling are regular activities. But glacier avalanche is not
114 considered as disaster component so far in the planning of infrastructure and
115 development projects as well as regular activities in the higher Himalayan region.

116

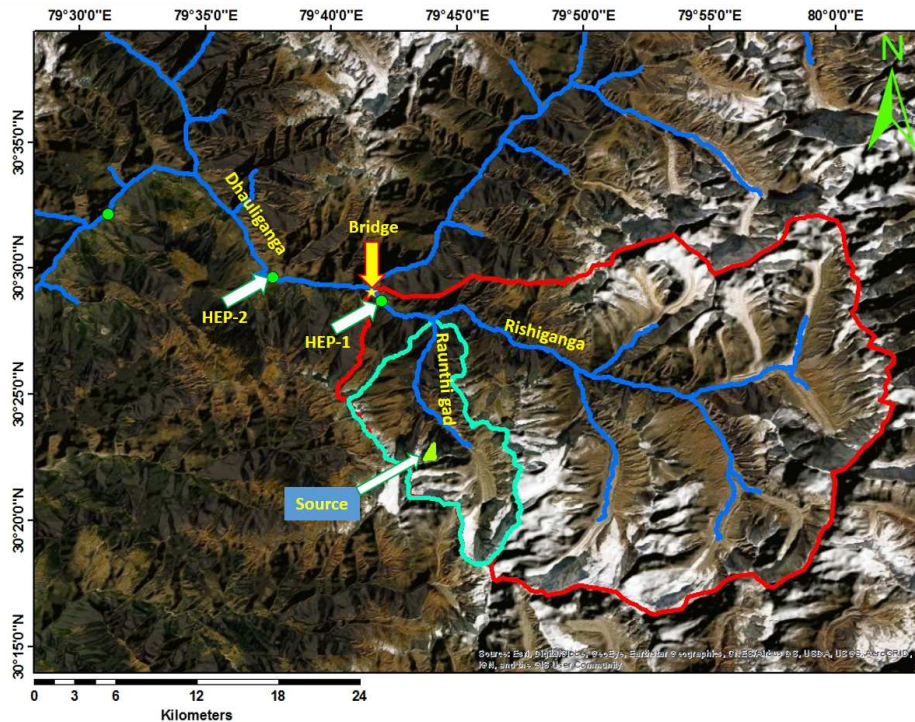
117 In the mountainous glacial environments, the catastrophic mass flows are an essential
118 geomorphic process that may pose a significant hazard to the infrastructure and the
119 communities living downstream (Patterson, 1994, Evans and Delaney, 2015). These
120 include a mass movement of glacial debris flows, ice rock avalanches, and outburst-
121 generated flows, occurring at a time when glaciers are shrinking in response to climate
122 change (Evans et al., 2009, Evans and Delaney, 2015). The 2002 event of Kolka
123 glacier detachment in the Caucasus mountain, southern Russia, is a vivid but rare
124 example of such catastrophic events (Evans et al., 2009; Haeberli et al., 2004; Huggel
125 et al., 2005). Closer home, the May 5th 2012 Seti river flood in Nepal initiated by the
126 detachment of rock mass at the height of 6700m a.s.l. from the south flank of
127 Annapurna IV and ended up as colossal debris flow (OI et al., 2014; Kargel et al.,
128 2014; Dwivedi and Neupane, 2013; Kim et al., 2017; Hanisch et al., 2013; Bhandary
129 et al., 2012). Rockfall induced debris flow of Piz Cengalo, south-eastern Switzerland
130 in 2017 (Mergili et al., 2020), the 2012 rock–snow avalanche in the Alps, Austria (Preh
131 and Sausgruber, 2015) and the 2012 multi-lake outburst flood in the Santa Cruz Valley
132 (Mergili et al., 2018) illustrate the potent threat of such events in the cryospheric
133 regions of world's mountains in a warming climate. In most of these events, the
134 ambiguity remains regarding the accurate flow volumes involved and the mechanism
135 of flow transformation, water source, etc. A detailed overview of these type of events
136 could be found in Evans and Delaney (2015).

137 **2.0 Study Area**

138 The Ice-rock avalanche by detachment of the hanging glacier situated at headwater
139 region of Raunthigad (Lat: 30°22'40.62"N, 79°43'57.66"E) in Chamoli district of
140 Uttarakhand. Raunthigad originates from the Trishuli glacier, and the snout of the
141 Trishuli glacier is around 1.5 km further ahead of the point where the ice-rock
142 avalanche hit the valley. The Raunthigad catchment has an area of 94 km² with a
143 glacier cover of 16 km². Raunthigad catchment extend from 2380 m a.s.l. to 7120 m
144 a.s.l. (Trishul peak) and joins with the Rishiganga basin. Rishiganga basin drains an

145 area of 686 km² and has 52 glaciers with 177 km² glacier cover. For precipitation,
146 snow, land surface temperature (LST) analysis and assessment of soil thermal regime
147 fluctuation, we drew an area of interest (AOI) of 3 km² around the hanging glacier on
148 the northern slope. The geology of the area comprises of Jutogh, Almora formation
149 and the area is close to Main Central Thrust (MCT) (WIHG,1992). Quartzite, marble
150 and garnet, granite gneiss etc., dominate this group.

151



152

153 Figure 2: The drainage map of the area showing the Raunthigad catchment and
154 potential source area of the ice-rock avalanche, Rishiganga catchment and
155 Dhauliganga and Alakananda rivers further downstream.

156

157 3.0 Methodology

158 3.1 Area change of the Hanging glacier

159 Glacier area change is estimated from 1985 to 2020 using satellite images and google
160 earth images. Table 1 show the satellite data description. Glacier boundary marked
161 manually, and area change is calculated. The area of the hanging glacier in 1985 is
162 also estimated from the Survey of India toposheet (53N/11, 1: 50,000).

163 3.2 Glacier volume estimation

164 Glacier volume estimation is carried out using the standard glacier area-volume
165 relationship:

$$166 \quad V = \alpha A^\gamma \quad (1)$$

167 An average value of 1.36 has been arrived for the scaling index γ from depth-sounding
168 (Bahr et al., 1997) and considered it as a global exponent. We used a volume estimate
169 of the glaciers from the glacier inventory of the Geological Survey of India (GSI), which
170 is based on the Muller's classification, to estimate the scaling constant as the scaling
171 constant could vary from region to region. We found that for glaciers with less than 2
172 km² area, the average scaling constant is 0.024, and for bigger glaciers, 0.027 gives
173 the best relationship between the variables (Thayyen et al., 2010, Unpublished report).
174 We used the following relationships to estimate the glacier volume in the present study
175 for a range of possible glacier volume.

$$176 \quad \text{Glaciers} < 2\text{km}^2, V = 0.024 A^{1.36} \quad (2)$$

$$177 \quad \text{Glaciers} > 2\text{km}^2, V = 0.027 A^{1.36} \quad (3)$$

178 Where volume, V in km³ and area, A in km²

179

180 **3.3 Land Surface Temperature of Hanging glacier catchment Raunthigad** 181 **catchment**

182 Moderate Resolution Imaging Spectroradiometer (MODIS) Land Surface Temperature
183 (LST) data was accessed from <https://lpdaac.usgs.gov/tools/appeears/>. All four daily
184 data points of LST (MOD11A1) from Terra and Aqua satellites (~10:30 AM, 10:30 PM
185 and ~01:30 PM and 01:30 AM) between 2002 to December 2020 (18 years) was
186 downloaded. The batches were consolidated separately by clipping over the hanging
187 glacier area of the Rishiganga basin. LST values in 4 grades with varying error (error
188 $\leq 1\text{K}, \leq 2\text{K}, \leq 3\text{K}$ and $> 3\text{K}$)

189

190

191

192 Table 1: Details of data products used in this study.

Sl. No.	Data Product Name	Period of Availability	Spatial Resolution	File Format	Remarks
1	Advanced Spaceborne Thermal Emission and Reflection Radiometer (ASTER) Global Digital Elevation Model	-	30 m	tiff	https://asterweb.jpl.nasa.gov/gdem.asp
2	High Mountain Asia 8-meter Digital Elevation Models	-	8 m	tiff	http://dx.doi.org/10.5067/KXOVQ9L172S2
3	Sentinel-2	5 Feb, 2021 (Pre-event); 10 Feb, 2021 (Post-event)	10 m	tiff	https://sentinels.copernicus.eu/web/sentinel/home
4	Planet labs imageries (as screen shots from website)	3,5 Feb, 2021 – 09 th Feb, 2021	3 m; 5 m	.jpg	https://www.planet.com/
5	Maxar Opendata Programme	10 Feb, 2021	3 m	.jpg	https://www.maxar.com/open-data/uttarakhand-flooding?utm_source=blog&utm_medium=organic&utm_campaign=Uttarakhand
6	Google Earth Pro data	1985; 2003; 2005; 2012; 2015; 2017; 2019	15 cm – 30 cm	.jpg	https://www.google.com/intl/en_in/earth/versions/

193

194 has been generated and built a continuous data series by incorporating the less
 195 accurate data in a hierarchical way (Yadav et al., 2020) . The remaining gap is filled
 196 by interpolation. The satellite-derived LST data could vary significantly with the Ground
 197 Surface Temperature (GST) data. To refine the LST data, we used 3 years (2016-
 198 2019) of rock temperature data generated in the Ladakh mountain range in western
 199 Himalaya (Fig. S1). Monthly regression equations were developed using the GST
 200 observation and MODIS LST for this site which provided a good match with
 201 observations ($R^2 = 0.92$, Fig. S1b). Using these monthly regression equation (Table
 202 S1), we generated the GST equivalent of LST for the avalanche area for further
 203 modelling of ground temperature regime using the GEOTop model (Endrizzi et al.,
 204 2014).

205 3.4 Precipitation over hanging glacier catchment and nearby stations

206 Precipitation changes in the region are analysed by using the station observation from
 207 Chamoli (30.293N, 79.56E) since 2000 and GPM IMERG Final Precipitation L3 1 day
 208 0.1 degree x 0.1 degree V06 (GPM_3IMERGDF) (Huffman *et al.*, 2020) (available at

209 <https://disc.gsfc.nasa.gov/>). The daily files from the datasets were clipped to the Ice-
210 rock avalanche site in the Raunthi catchment.

211 **3.5 Snow over change over the hanging glacier area**

212 Accurate snow cover assessment in the monsoon dominated regions of the Himalaya
213 is a challenge due to persistent snow cover. A new methodology proposed by Singh
214 et al. (2019) is used to generate the elevation-depended snow cover change since
215 2000. For generating daily Snow cover area (SCA), MODIS daily Snow cover
216 products, e.g. MOD10A1 and MYD10A1 version 6 (V6) from Terra and Aqua were
217 downloaded from the NASA earth data website (<https://search.earthdata.nasa.gov>)
218 and re-projected into UTM WGS84 projection. All the initial classes of the downloaded
219 products are reclassified into three major classes (0=cloud, 1=non-snow, and 2=snow)
220 as defined in Table S1.

221

222 ALOS World 3D, distributed freely by the Japan Aerospace Exploration Agency
223 (JAXA) is downloaded to the same extent as MODIS SCPs from the open topography
224 website (<https://portal.opentopography.org/dataCatalog?group=global>). Downloaded
225 ALOS Word 3D DEM is resampled and re-projected using bilinear interpolation to have
226 the MODIS SCPs projection and spatial resolution. This resampled DEM is then used
227 for the generating slope direction (Aspect) and elevation Zone map. Aspect map is
228 classified into four distinct directional classes (North-east, South-east, South-west,
229 and North-west). DEM is classified into 10 zones with a range starting from <2000 m
230 as 1st zone, after that, subsequent zones are of 500 m elevation interval up to 6000
231 m elevation. Elevation of More than 6000 m is classified as 10th zone. Sub watershed
232 data is generated from the same DEM using open source hydrological analysis tools.
233 After generating all these files, daily cloud-free SCPs are generated by processing
234 MODIS SCPs using the methodology proposed by Singh et al. (2019). The
235 methodology proposed by Singh et al. (2019) consists 5 successive logical steps
236 consisting of Temporal filtering, Combining Terra and Aqua SCPs, Aspect wise mean
237 Snowline and No-Snow line altitude conditioning for sub-watershed and elevation
238 based moving filter. Temporal filtering is employed for the same period as suggested
239 by Singh et al. (2019) for Himalayan terrain. After completing all the steps, Cloud free
240 SCPs received from the fifth step are clipped using the study area boundary and
241 further used to generate elevation zone wise daily SCA (in %) statistics.

242 **3.6 Modelling of Soil thermal regime**

243 For the past two decades, the soil temperature at the study site was simulated using
244 the GEOtop (Endrizzi et al., 2014). Only the soil part of the model was used with water
245 transport disabled. The model was run in a one-dimensional model with a Dirichlet
246 boundary condition at the top and a Neumann boundary condition at the bottom. The
247 MODIS land surface temperature was used at the top, and flux of 0.0 W m^{-2} was used
248 at the lower boundary. The simulation of soil temperature is carried out for high
249 diffusivity conditions with a heat capacity equal to $2.25 \times 10^6 \text{ J m}^{-3} \text{ K}^{-1}$ and the thermal
250 conductivity equal to $4.0 \text{ W m}^{-1} \text{ K}^{-1}$. Due to the non-availability of parameters, the
251 model parameters typical to granite rocks available in the literature were used (Drury,
252 1987; Gubler et al., 2013). The depth of the modelling soil column was kept up to 100
253 m and was initialised with an initial temperature of $-2 \text{ }^\circ\text{C}$. Before analysis, the model
254 was run 50 times to attain thermal equilibrium (Pogliotti, 2011; Wani et al., 2020).
255 Further details about the experimental design could be found in Wani et al. (2020).

256

257 **3.7 Flood modelling**

258 The design flood hydrograph of the flood event was generated using Soil Conservation
259 Service (SCS) dimensionless unit hydrograph (DUH) methodology (SCS, 1964; Jeng,
260 2006; Thayyen et al., 2013). SCS, now Natural Resources Conservation Service
261 (NRCS) developed a DUH based on the analysis of many watersheds. It approximates
262 the flow from an intense storm from a small watershed. The SCS hydrograph arbitrarily
263 has 100 units of flow for the peak and 100 units of time for the duration of flow. The
264 SCS DUH consists of 37.5% of the total runoff volume before the peak discharge and
265 the remaining volume after the peak discharge occurs. The total base of the DUH is 5
266 times the time to peak (T_p). It has 19 constant ordinates that represent percentages of
267 flow and time. The DUH is scaled to various size storms events using three conversion
268 factors. To develop the design hydrograph, we required the likely total runoff volume,
269 storm duration, and stream dimension.

270 We also attempted one-dimensional unsteady flow hydraulic modelling using HEC
271 RAS 5.0.7 using the design hydrograph discussed above up to the NTPC site located
272 at Tapovan to understand the flow velocity and flow depth.

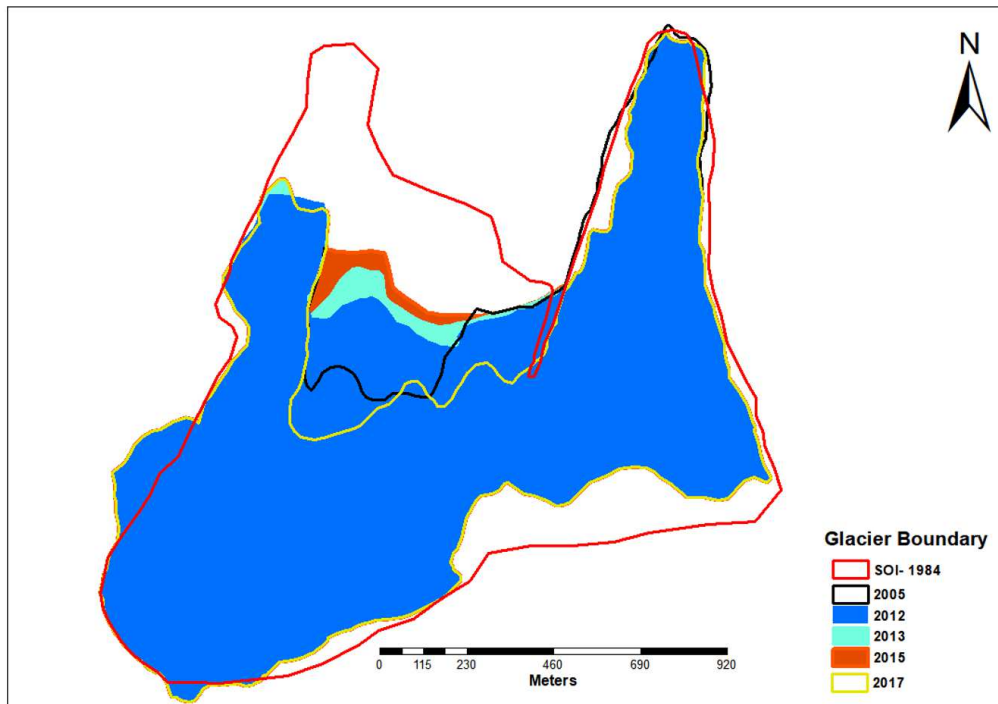
273 The freely available digital data of Advanced Spaceborne Thermal Emission and
274 Reflection Radiometer (ASTER) Global Digital Elevation Model of 30 m resolution is
275 used to delineate Rishiganga and Raunthigad watersheds, generation of elevation
276 profiles, drainage lines, x-sections, and other hydrodynamic parameters. Multi-date
277 remote sensing data of Sentinel-2 for pre-event and post-event were used to assess
278 the extent of damage due to the event. Sentinel-2 has 10 m ground resolution and
279 twelve spectral bands of a different wavelength. One scene for each of the pre-event
280 (6th - 7th Feb., 2021) and post-event (8th – 9th Feb, 2021) of the avalanche initiation
281 area were used for the analysis. We have cross validated the results using the fine-
282 resolution data (3 m x 3 m) shared by the Planet lab. Further, open data (3 m x 3 m)
283 from the Maxar technology programme for 10 Feb., 2021 was used for analysing the
284 post-disaster stream morphology changes from the source area to 23.58 km till HEP-
285 2 site at Tapovan.

286

287 **4.0 Results and Discussion**

288 **4.1 Area change of the Hanging glacier and early indicators**

289 Like any other glacier, a hanging glacier is a dynamic ice mass with internal flow and
290 deformation in response to the climate forcing and mass balance regime. As glaciers
291 move under gravity, the mountain slope on which it sits become a critical factor. As
292 per the survey of India (SOI) topo sheet of 1984, this hanging glacier had an area of
293 1.7 km² which reduced to 1.23 km² in 2017. The glacier has right, center and left lobes
294 in which most of the change during these 33 years was recorded at central and left
295 lobes, with the right lobe remains at its place. This suggests that the right lobe was in
296 the steady-state condition during this period (Fig.4) with a flat glacier tongue which
297 flows from 5555 m a.s.l. to 4700 m. The glacier occupied a mountain slope having an
298 average slope of 35°. The headwall above the bergschrund have a higher slope of
299 49°. The central part extended from 5788 m a.s.l. to 5500 m at lower margins, and the
300 left lobe extending from 6040 m to 5180 m a.s.l. The most visible signs of the climate
301 forcing on a glacier are its area change over a period. From 1984 to 2003, the glacier
302 area reduced to 1.38 km² from 1.7 km² (Fig. 4).



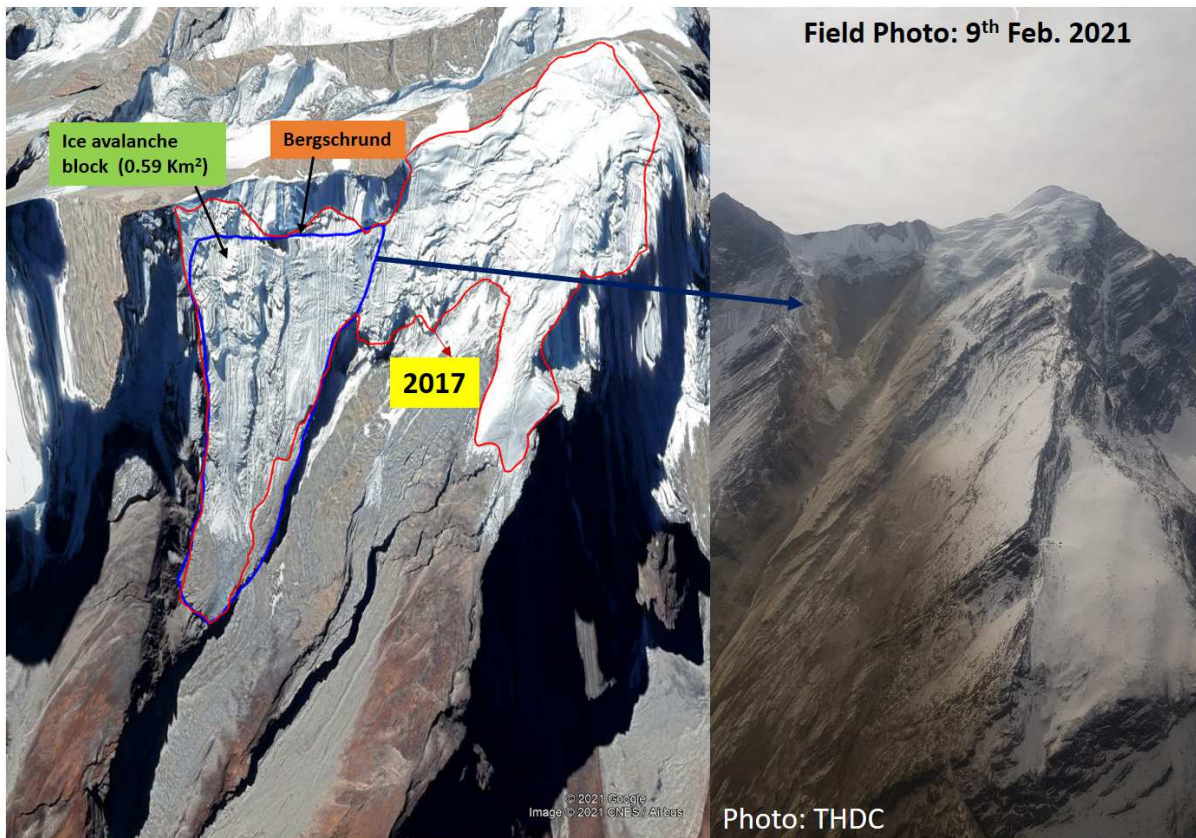
303

304 Figure 3: Glacier area change since 1984 showing steady-state conditions of right
 305 detached lobe for 33 years and significant area change for left central lobes

306

307 From 2005 the glacier experienced further area loss to 1.27 km². However, by 2012
 308 central glacier lobe advanced by around 236 m and recorded a corresponding
 309 increase in area to 1.3 km². The advancement of the central lobe continued during
 310 2013, 2014 and 2015 reached 1.351 km² in 2015. Overall advancement of the central
 311 part of the glacier from 2005 to 2015 was around 330 m. This central part of the glacier
 312 was sitting over the steep and plain bedrock. A close look at the surface conditions of
 313 the glacier shows a certain degradation of the glacier at 'C' area with the development
 314 of multiple cracks in 2012 and 2015 images (Fig. S2). It suggests that the glacier has
 315 either moved from the quiescent phase to the active phase during the period
 316 (Rothlisberger, 1987) or advanced due to enhanced accumulation. Between 2016
 317 and 2017, all the glacier area which showed advancement till 2015 has got detached,
 318 and the glacier area reduced to 1.23 km², recording an area loss of 0.121 km² and
 319 remain more or less same way till 2020 with little shrinkage of the central part. This
 320 analysis suggests that the central lobe of the glacier was continually under recession
 321 during the last 3 decades with surge like advancement and sudden degradation. The
 322 right lobe, which remained in its position through these 33 years, got detached on 7th

323 February 2021 and caused the catastrophic flood. Figure 4 shows the detached part
324 of the hanging glacier and a post-event field photo showing its geometry. This shows
325 that the glacier is detached from the bergschrund and the sharp edges of the crown
326 suggest that the glacier was not sliding at its bed which is also indicated by the steady
327 positioning of the right lobe for the past 33 years. The detachment of the central lobe
328 in 2016 seems to indicate the vulnerable conditions of this glacier.



329

330 Figure 4: A) Hanging glacier in google earth image of 2017. The detached right lobe
331 is marked blue. B) Heli photo of 9th February 2021 of the site showing detachment of
332 the glacier creating an ice-rock avalanche. (Photo courtesy, THDC)

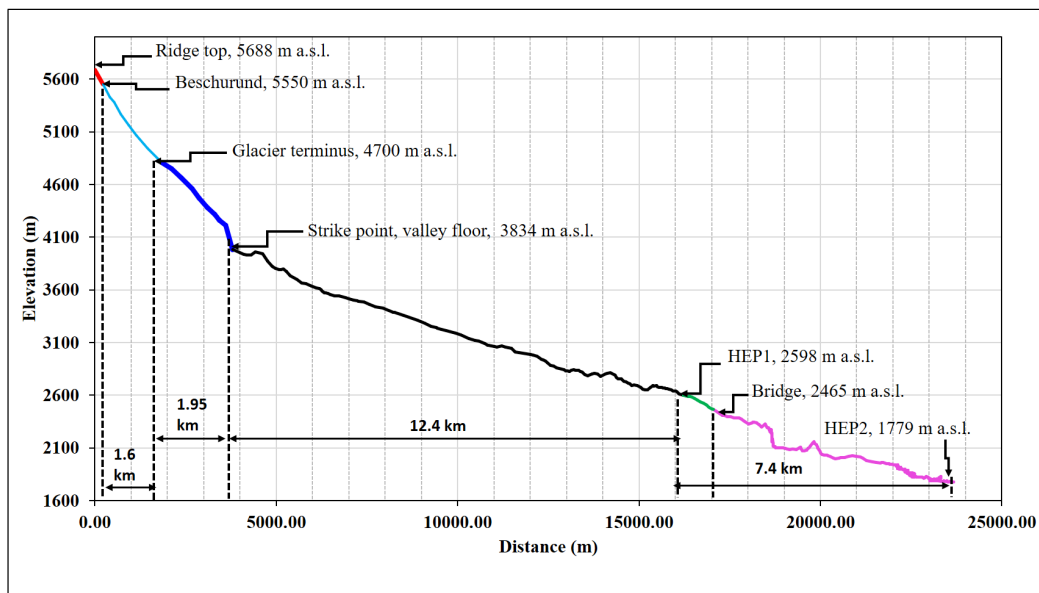
333 4.2 Glacier volume estimation and other water sources for debris flow

334 The total area of the Hanging Glacier in 2019 was 1.23 km², and the area of right lobe
335 of the glacier, which fell off on 7th in 2019, was estimated to be 0.59 km² (48%). Using
336 the area-volume scaling, the volume of the detached part of the glacier is estimated to
337 be in the range of 11.7 to 13.2 x10⁶ m³. Snow over the glacier is not accounted for this
338 estimation. Since there was heavy snowfall in the 2019 winter and two days before the
339 event in 2021, it is suspected that significant snow accumulation happened over the

340 glacier. The surface features of the hanging glacier prior to the avalanche in the
341 satellite image of 5th December 2020 show thick snow accumulation over the glacier
342 (Fig. S3). The volume of water in the debris flow could be higher as about 14 km runout
343 stretch of the avalanche, till it joins Rishiganga river was snow-covered and could be
344 incorporated in the debris flow matrix. Another source of water is the soil moisture as
345 reported in the events reported earlier from other parts of the world by entrainment of
346 large quantity of soil and rock (Evans, 2017), eventually turning it into a debris flow
347 and facilitate melting of the huge glacier ice mass with frictional heat generated during
348 its high velocity down slope movement. This particular aspect needed detailed study
349 and not attempted in this preliminary assessment.

350 **4.3 Ridge and valley slope profile**

351 Figure 5 show the elevation profile drawn from the ridge top of the Raunthi glacier area
352 to the HEP 2 at Tapovan, traversing a distance of 23.58 km. Above the bergschrund,
353 a 138 m section with a steep mean slope of 49° connects to the ridge at 5688 m a.s.l.
354 On the left, the glacier flows down from Raunthi peak at 6063 m a.s.l. The right lobe
355 of the glacier is 1.6 km long and with a mean slope of 35 degrees with its terminus at
356 4700 m a.s.l. The avalanche travelled a distance of 1.95 km through bedrock with a
357 mean slope of 33° before striking the valley floor 3834 m a.s.l. The Ice rock avalanche
358 converted into a debris flow during its transport through the valley with 7° mean slope
359 for another 12.4 km till HEP 1. Between the bridge site and HEP 2 the average channel
360 slope was 5.6°.



361

362

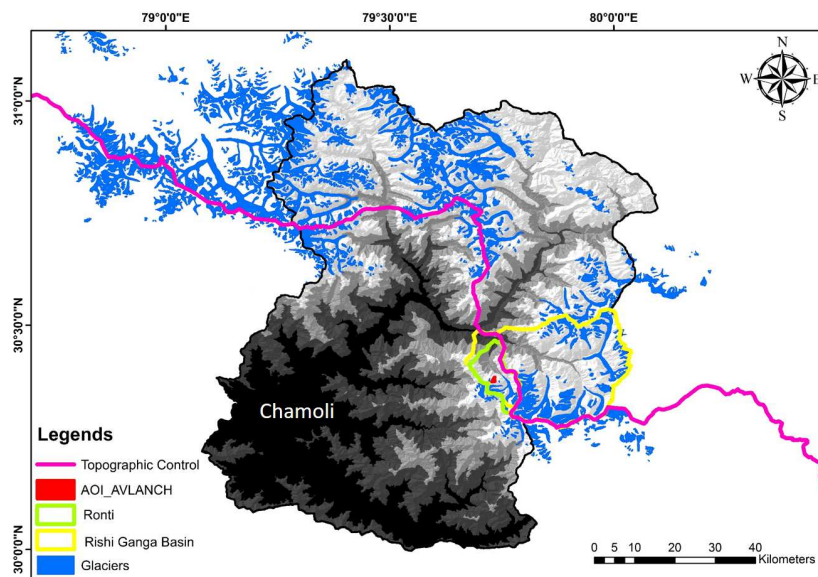
363 Figure 5: Elevation profile for the stretch between ridge top to HEP 2 at Tapovan.

364

365 4.4 Precipitation over hanging glacier catchment and Raunthi Gad

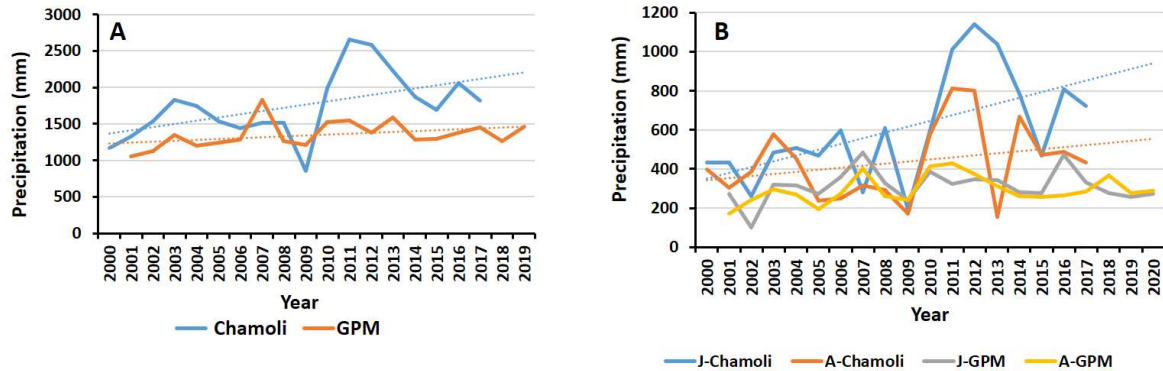
366 Precipitation and forms of precipitation, liquid or solid, is critical for glacier behaviour
 367 and thermal regime of surrounding periglacial areas. The southern slopes of the
 368 Himalaya are highly influenced by the monsoon precipitation and show elevation and
 369 topographic dependencies (Bookhagen, 2007, 2010). As this glacier occupied an
 370 elevation of 4695-5550 m a.s.l. It is expected that monsoon precipitation can occur as
 371 rain or snow or as a mixture depending on the prevailing atmospheric conditions. The
 372 Raunthigad catchment, where the glacier is situated, forms the northern boundary of
 373 the monsoon influence zone of the southern slopes (Fig.6), and the topographic
 374 control (TC) (Bankim et al., 2020) runs through the northern ridges of Raunthi gad
 375 reaching up to 7120 m a.s.l. (Trishul peak). This is a critical factor as monsoon
 376 dominated areas of Uttarakhand Himalaya have less than 20% glaciers compared to
 377 the monsoon deficit zone in the north of the TC, suggesting less favourable conditions
 378 of southern slopes for glaciers. This also demonstrated by shallower temperature
 379 lapse rates at the monsoon dominated glacier areas suggesting a high energy system
 380 through latent heat release of precipitating monsoon (Thayyen et al., 2005, Thayyen
 381 and Dimri, 2018, Bankim et al., 2020). Nearest high elevation precipitation station

382 located at Chamoli (2640 m a.s.l.) experience annual precipitation in the range of 2659
383 mm to 850.8 mm. Monsoon precipitation in July and August constituted 53% of annual
384 precipitation during the 2000-2009 period, which increased to 65% 2010-2017 period.
385 Annual precipitation shows an increasing trend with a steep increase since 2010 (Fig
386 7a). Most of this increase is attributed to July, August precipitation (Fig 7b). Satellite-
387 derived precipitation data (GPM) of 2001-2019 for the Raunthi gad ice-rock avalanche
388 grid show annual precipitation of 1352 mm with 998 mm w.e. (74%) precipitation
389 occurring in summer months (May to October) and average 354 mm w.e. in during
390 winter period. Annual precipitation derived from GPM for glacier area also shows a
391 nominal increasing trend as well as for monsoon months of July, August as
392 experienced at Chamoli station (Fig 7). Both the data set suggests an increase in
393 monsoonal precipitation in the region, especially since 2010. GPM data also suggests
394 2019 experienced the heaviest winter precipitation since 2001 with 577.7 mm w.e. of
395 snowfall which is corroborated by snow cover assessment of the region (Mritunjay et
396 al., 2019).



397

398 Figure 6: Topography control (TC) dividing the monsoon and monsoon deficit zone in
399 Uttarakhand. Note the location of the Raunthigad catchment and the location of the
400 avalanche zone southern side close to the TC. (Modified after Bankim et al., 2020)



401

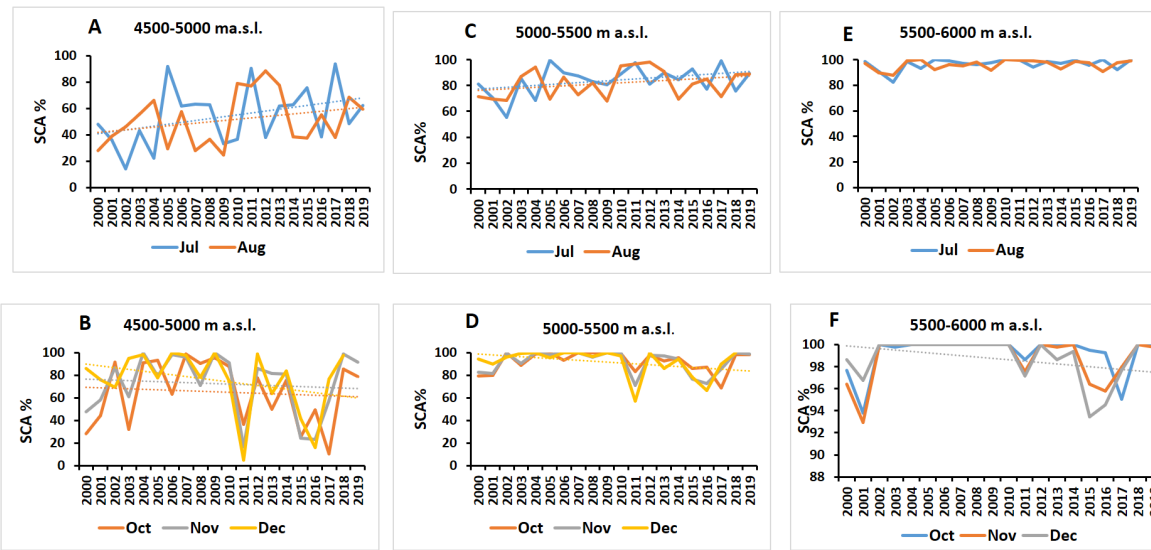
402 Figure 7: Precipitation over the region showing an increasing trend for the station and
 403 GPM data A) Annual precipitation B) July and August precipitation.

404

405 **4.5 Snow cover change over the hanging glacier area**

406 Change in the snow cover characteristics is a critical aspect that alters the temperature
 407 regime of high elevation non-glaciated land surface and dynamics of glaciers through
 408 mass balance. Elevation depended snow cover variations were observed in the nearby
 409 Bhagirathi basin from 2000-2019 period showing declining snow cover trend in
 410 December between 3000-6000 m a.s.l. elevations and an increasing trend in June for
 411 4500-6000 m a.s.l. elevations (Mritunjay et al., 2019). Snow cover variation is
 412 assessed over the hanging glacier area and elevations as well as for the Raunthigad
 413 catchment using the modified cloud removal algorithm (Mritunjay et al., 2019). The
 414 study shows an increasing snow cover trend in July and August for elevation band
 415 4000- 5500 m a.s.l. and a declining trend in snow cover in September to November
 416 months for elevation between 4500-6000 m a.s.l. (Fig 8), especially after 2010. The
 417 increase in snow cover is in tandem with the increase in precipitation observed above,
 418 and decrease in snow cover during September, October and November in also match
 419 with the increase in LST observed during these months (section 4.6). Summer snowfall
 420 in lower elevations is always a mix of rain and snow and do not sustain over a warm
 421 land surface in summer for a longer duration. Daily snow cover assessment shows
 422 short duration snow cover during these summer months. The declining snow cover
 423 trend of September to November support this observation. However, summer snow
 424 on the glacier surface could stay longer, depending on the rain-snow ratio in the
 425 precipitation and could impact the glacier mass balance positively. The declining trend

426 in snow cover during pre-winter months and increasing trend in summer monsoon
 427 months becomes highly significant after 2010.



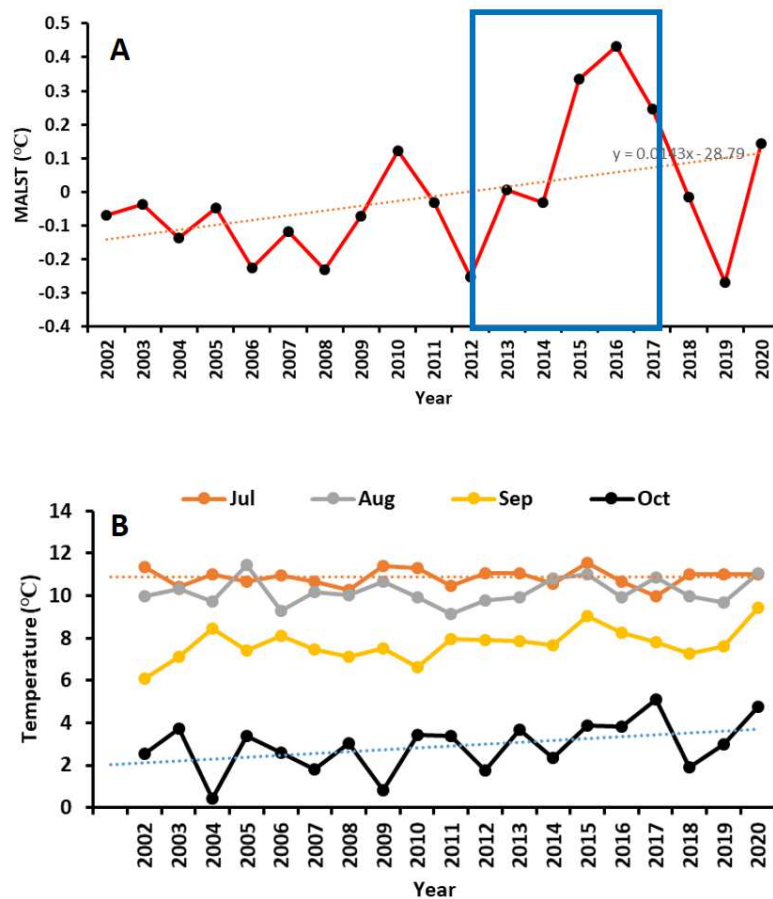
428

429 Figure 8: Elevation-depended seasonal change in snow cover in the glacier elevations
 430 of Raunthi gad showing an increasing trend in monsoon months and decreasing trend
 431 in October, November and December months. Decreasing trend is significant since
 432 2010.

433 **4.6 Land Surface Temperature of Hanging glacier catchment Raunthi gad**
 434 **catchment**

435 Land surface temperature (LST) of 3 km² area around the hanging glacier, most of it
 436 covered by exposed bedrock, is studied for evaluating the site-specific LST changes.
 437 The southern slope of the ridge is fully exposed in summer, and the permanent snow
 438 and ice are restricted to the northern slopes close to the ridge elevations. Mean annual
 439 LST during 2001-2020 range between -0.3 to 0.4 °C period and show a steady rise
 440 from low LST of -0.3 °C in 2012 to 0.4 °C in 2016 (Fig. 9a). July and August months
 441 recorded a maximum LST of 11.5 °C and a minimum of -11.7 in January. LST of July
 442 shows an insignificant negative trend, and August show no specific trend. LST of
 443 September and October represent temperature regime at the end of the water year,
 444 which also shows a significant rise from -1.9 °C in 2009 and 9.1 °C in 2017 (Fig. 9b).
 445 LST increase in September and October months is mainly attributable to the reduced
 446 snow cover in these months. This clearly indicates warmer surface conditions build up
 447 around the hanging glacier area since 2012, facilitating the basal ice melt around the

448 margins of the hanging glacier, especially at the lowermost zone, which seems to be
 449 firmly coupled with the bedrock earlier. This can also explain the surge like
 450 advancement of around 330 m noticed in 2015 as basal melting due to warmer
 451 temperature reduces the basal resistance and further warmed up the glacier ice, which
 452 facilitated the enhanced flow of the central lobe of the glacier (Part D in Fig S1). This
 453 advanced section got removed during the 2016-2017 period suggesting this section
 454 probably detached and fell as a block rather than melting away. Considering the LST
 455 warming since 2012, this could be considered as a precursor to the present event. The
 456 rock exposure caused by this event probably helped further the warming of the glacier
 457 frontal area.

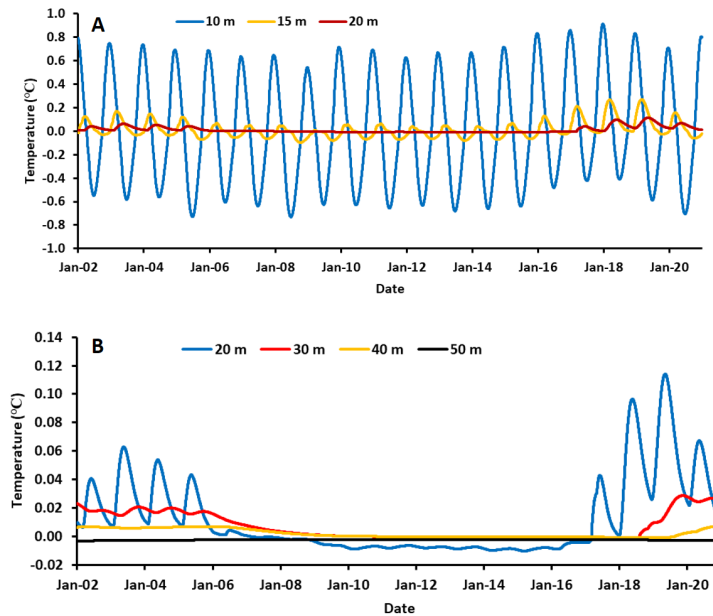


458
 459 Figure 9: a) Mean Annual LST variation around hanging glacier area during 2002-2020
 460 b) LST variation during July, August, September and October showing a significant
 461 rise from 2012 to 2016 also reflected in October LST. Peak monsoon months show no
 462 increase in LST.

463 **4.8 Ground thermal regime variation**

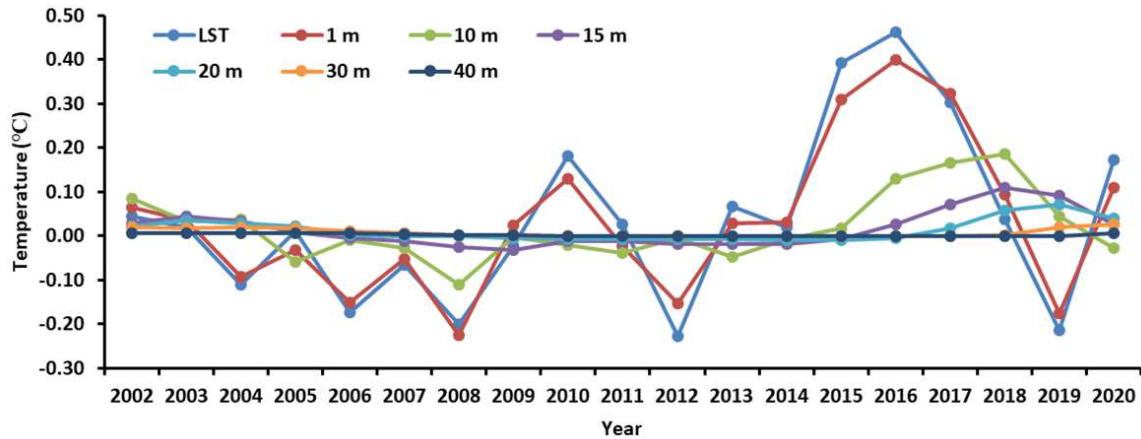
464 The response of small glaciers and ice aprons situated over the bedrock on the
465 mountain slope is impacted by surface accumulation and the thermal regime of the
466 bedrock. Bedrock warming could lead to basal melting and eventual decoupling of the
467 glacier from the bed. As this glacier is situated in the elevation band of 4695-6000 m
468 a.s.l, the possibility of the existence of permafrost areas and its thawing under a
469 warming climate also could lead to slope failures. Recent studies in the Ladakh
470 Reference Himalaya suggests permafrost condition above 4900 m a.s.l. Hence, a
471 preliminary attempt is made to assess the soil thermal regime of the area surrounding
472 the hanging glacier. In the absence of any ground-based temperature data from the
473 region, daily refined LST regressed to the ground surface temperature of the 2002-
474 2020 period and used to model the soil thermal regime up to 100 m. The thermal
475 envelop curve for 20 years under high diffusivity condition suggests that the area has
476 warm permafrost below 50 m with mean annual rock temperature at 50 m range
477 between -0.0021 to -0.0031 °C (Fig. S4). The warm permafrost that is defined as
478 permafrost with temperature at or higher than -1.0 °C (Cheng and Wu, 2007; Wu and
479 Zhang, 2008; Wu et al., 2010; Changwei et al., 2015). At 40 m, this range changes to
480 0.0061 to -0.0006 °C suggesting non-permafrost conditions. However, using low
481 diffusivity values, the region shows permafrost condition at a depth of 10 m with an
482 annual temperature range of -0.074 to -0.126 °C. The site photos suggest that rock
483 mass detachment occurred from deeper zones. The standard values of rock
484 parameters for granite match with the high diffusivity condition. Hence we considered
485 only high diffusivity values for further analysis. The modelled daily temperature
486 variations at 10, 15, and 20 m depths show seasonal temperature variations
487 suggesting the conducive seasonal thermal variation for frost cracking up to 10-15 m
488 depth (Fig. 10a). Figure 10b shows low amplitude seasonal variations in temperature
489 at 20 m. This is due to a sustained sub-zero mean annual surface temperature which
490 converted to high amplitude seasonal fluctuations once the surface temperature
491 becomes positive and rising since 2012. At 40 m, this variation reflected as sustained
492 sub-zero (-0.0001 to -0.0006 °C) from 2011 to 2018 period and moved to the positive
493 regime from 2019 to 2020 up to 0.0052 °C. The delayed response of rising surface
494 temperature at the deeper layers are clearly illustrated in Figure 11. At 40 m, the
495 response of temperature increase (2012-2016) reached after a 4year delay. This shifts

496 between freezing and thawing regime at this depth under warm permafrost conditions
 497 probably made this depth more vulnerable for detachment. As discussed earlier, below
 498 50 m depth permafrost conditions prevailed during the past 20 years, and depth
 499 between 40 to 50 m provided favorable conditions for the present detachment forced
 500 by warmer weather conditions since 2012 suggesting clear signals of climate forcing
 501 on the present event (Fig. S5).



502
 503 Figure 10: a) Modelled monthly mean temperature variation at a) 10,15 and 20 m
 504 and b) 20, 30, 40 and 50 m showing the seasonal changes and delayed warming
 505 towards deeper depths

506
 507 As the glacier is placed over the bedrock, significant seasonal variations in
 508 temperature regime are observed, with rock surface temperature rising to 18 °C in the
 509 summer months. The month of October showed a higher rate of warming (Fig. 9a).
 510 This high temperature of the rock mass surrounding the hanging glacier melts the
 511 glacier margins and helps it decoupling from the bed. At 10 m, also peak annual
 512 temperature is the range 0.6 to 0.8 °C and susceptible to melting under prevailing
 513 conditions. The surface warming is particularly sharp in October (Fig. 9b Oct.),
 514 especially during the 2009-2017 period when October LST shows a sharp increase
 515 from 0.8 °C to 5.1 °C.



516

517 Figure 11: Delayed response of deeper depth to LST increase from 2012, which
 518 peaked in 2016. A 4year delay at 40 m forced the highest temperature between 40-50
 519 m during December-February.

520

521 Refreezing of this meltwater further melts the basal ice by the latent heat release.
 522 Recurrence of this process over 10 or more years could have widen the rock fissures
 523 and reduced basal adhesion. For thick temperate glaciers, a thin film of water at the
 524 basal zone is very normal, maintained by the pressure melting even in winter months.
 525 At 40 m and below it is observed that an incremental increase in the temperature
 526 during the 2002-2020 period and a sharp increase in temperature at 40 m depth from
 527 sub-zero to 0.008 °C (Fig. S5). This could be a factor that facilitated this event
 528 happening in February. It is possible that the depth assessment of active layer may
 529 vary as we used LST proxy in place GST.

530 **5. Discussion**

531 Considering the deep scar with unknown depth associated with the hanging glacier's
 532 right lobe, which detached on 7th February, 2021, it could be a case related to the
 533 sudden movement of the hanging glacier linked to basal sliding. Glacier ice thickness
 534 and surface slope (α) are the two important parameters determining the basal shear
 535 stress (τ_b),

536
$$\tau_b = \rho gh \sin \alpha \tag{4}$$

537 where ρ is glacier ice density, g is the gravitational acceleration. In general, glacier
 538 flow constitutes differential movement within the ice by internal deformation and sliding
 539 of the glacier on its bed illustrated by the following equation (Paterson, 1994):

$$540 \quad u = Ah^{n+1}\sin^n\alpha + Bh^m\sin^m\alpha \quad (5)$$

541 u , is velocity under non-steady flow conditions, h is ice thickness, α is glacier surface
 542 slope, and A , B , m and n are constants. The first term represents the differential
 543 movement within the ice, and the second represents the basal sliding. The well-
 544 defined geometry of the scar suggests that the glacier was firmly frozen to its bed with
 545 boulder entrainment so far without any basal sliding. The apparent stability of this
 546 particular section that fell off had a well-defined ablation tongue that flowed down to
 547 the lower elevation (4695 m a.s.l.) compared to the central lobe of the frontal glacier
 548 region (5500 m a.s.l.). In the case of basal ice containing rock debris, the effective
 549 basal shear stress is $\tau_b = \tau - \tau_f$, where τ_f is the frictional drag stress counteracting
 550 the shear stress (Paterson, 1994). In the present case, it could be the case of $\tau_b < \tau_f$
 551 prior to this event that held the glacier firmly in its place so far. The basal drag stress
 552 is formulated as (Sohomaker, 1988, cf: Patterson):

$$553 \quad \tau_f = \mu BC\eta\hat{w} \quad (6)$$

554 where μ is the coefficient of rock-rock friction, C is the debris concentration, B is a
 555 parameter with dimension m^{-1} describing the characteristic of the bed, η is effective
 556 viscosity of ice and \hat{w} is the average component of ice velocity perpendicular to the
 557 mean bed. Survey of India toposheet ,1984 mapped this glacier covering 1.7 km^2 of
 558 area, While the central and left lobes receded significantly during 1985-2017 (Fig. 3).
 559 The left lobe, which detached, showed no recession or advancement, suggesting that
 560 this section probably remained under steady-state flow conditions during the period.
 561 Thus the equilibrium condition is governed by (Patterson, 1994):

$$562 \quad -\rho gh \frac{dh}{dx} \delta x + (\rho gh \sin \beta) \delta x - \tau_b \delta x = 0 \quad (7)$$

563

564 This condition facilitates “over deepening” especially if the glacier occupies bed rock
 565 with a steep slope and provide vulnerable zones under prevailing geology. The Main
 566 Central Thrust (MCT) run close to the Raunthi catchment and is tectonically highly
 567 active under the zone-5 category. Hence, for the last more than hundred years, glacial

568 processes over this fragile zone might have facilitated significant over deepening
569 under this glacier. The overdeepening of the glacier bed occurs as shear stress at the
570 bed is determined by the surface slope. Ice flow is in the direction of maximum surface
571 slope, even if the bed slope is in the opposite direction (Patterson, 1994), if such a
572 situation exists due to local geological factors. The overdeepening occurs most where
573 maximum ice flow occurs and that usually happens at the equilibrium Altitude (ELA)
574 for small glacier with a steep slope.

575 It is observed in some instances that the product of erosion can build up at the glacier
576 bed, and lips of cirque and over deepening are coated in sediments (Hook, 1991 and
577 Alley et al., 1999). The erosional process at the glacier bed is modelled by MacGregor
578 et al., 2009 as below:

$$579 \dot{\epsilon} = (C_3 \times \psi_{sed} \times u_{slide}^2) + (C_4 \times u_{slide} \times \sin \beta) - (C_5 \times (\tan \alpha / (2 \times \tan \beta))) \quad (8)$$

580 the first term represents abrasion, the middle term represents quarrying, and the third
581 term represents negative feedback on quarrying based on local thickness of sediment
582 (till). In the present situation, abrasion was not probably taking place as sliding of the
583 glacier over long period of time is the pre-condition for significant abrasive erosion.
584 Here, plucking or quarrying is the dominant process where the overdeepening process
585 already provided significant rock mass attached to the glacier body, and any situation
586 facilitating or initiating glacier sliding can move the material. Quarrying is a function of
587 slope, and sliding velocity (MacGregor, 2009) and the steep slope of the present
588 glacier is a facilitating factor for the process. These are long-term glacial processes
589 under which glacial landforms are formed and well established in the glaciology
590 literature. Here, the changes in the regional climate as we observed during the past
591 20 years probably played a critical role in facilitating the sliding of the glacier leading
592 to the ice-rock avalanche due to glacier detachment.

593 **5.1 Role of recent changes in the regional climate**

594 Recent warming at the high elevation region seems to have resulted in the differential
595 response at two closely placed elevations. Increased precipitation in summer
596 monsoon months of July and August as evident from the precipitation data is one of
597 the critical factors. Part of this increased precipitation falls as snow, as evident from
598 the snow cover assessment as glacier elevations show an increase in snow cover

599 during July and August. This monsoon snow over the non-glacier area melts away
600 faster in a warm ground thermal condition as July and August LST range between 12
601 °C to 17.9 °C. This situation leads to an observed decreasing trend in snow cover in
602 September, October and November (SON) months and a corresponding increasing
603 trend of LST in October. The impact of reducing snow cover in the region is also
604 reflected in the cancellation of the Auli (a nearby ski slope) winter games in 2012,
605 2013, 2015 and 2016 (<https://bit.ly/38MfFgz>). The snow that falls over the glacier,
606 especially in the higher elevation, reduces the glacier melt and eventually increases
607 the glacier thickness in the accumulation zone, forcing incremental shear stress over
608 the glacier and at the glacier bed, facilitating faster movement. On the other hand,
609 increasing ground thermal regime due to regional warming, reduction in snow cover
610 and exposure of more bedrock area due to glacier wastage all facilitate increased
611 basal melting, especially at the glacier margins leading to reduce the basal adhesion
612 facilitating the glacier sliding. Permafrost identified in the area also played a crucial
613 role in facilitating the ice–rock avalanche. Changing active layer dynamics of the
614 permafrost under warm land surface conditions could enhance the frost cracking of
615 the bedrock fissures. Additional water from enhanced monsoon precipitation over the
616 region might have exacerbated these processes by providing more water to the
617 system. Annual freezing and thawing of the ~40 m active layer under warmer and wet
618 conditions probably exacerbated the weakening of the basal adhesion. In some
619 situations, frost cracking is found to be most active under a Mean Annual Ground
620 Surface Temperature (MAGST) between +4 °C and - 7 °C (Savi et al., 2021). In the
621 present case, the LST proxy of MAGST range between -0.3 to 0.4 °C and remain within
622 the zone of active frost cracking.

623

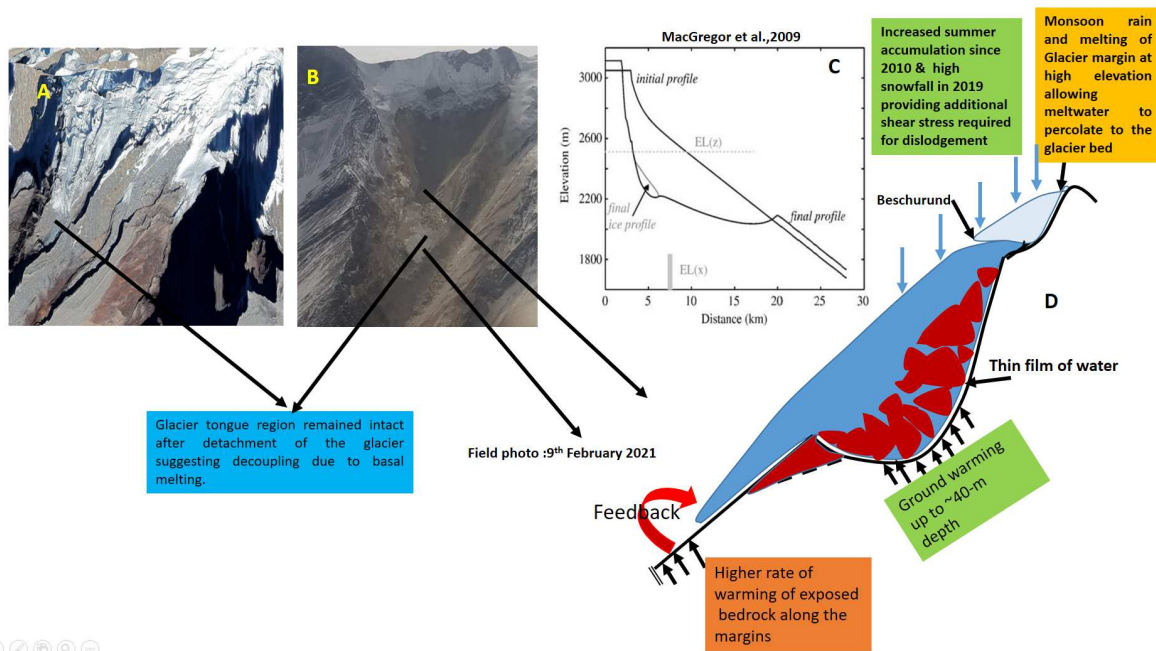
624 The effect of the enhanced ground thermal regime since 2010 is evident and visible at
625 the glacier zones where the glacier is not anchored over the bedrock as seen in the
626 advancement of the central lobe of the glacier sitting over the plain bedrock surface in
627 2012 with reference to its 2005 position. Development of thin film of basal water due
628 to warming of the ground thermal regime as showed earlier could change the bed
629 characteristics, B (Eq. 6) and lubricate the ice-bedrock interface and reduce the rock-
630 rock friction, μ allowing the basal slip to happen. Hence, an increasing trend in the
631 mean annual LST, especially from 2008 to 2016, from -0.2 °C to 0.4 °C could be a
632 critical factor as it further translated into the warming of ground thermal regime and

633 associated basal and glacier margin melting. This is clearly visible in the advancement
634 of the central lobe of the glacier (2012-2015) facilitated basal sliding without any
635 significant basal drag due to basal melting because of warming bedrock coinciding
636 with the LST warming. This resulted in an advancement of 220 m between 2005 and
637 2012, which increased to 264 m in 2013 and 320 m in 2015, and eventually the
638 detachment of about 435 m long section between 2015 and 2017 (Fig. 3). Bedrock
639 slope in the range 33° probably assisted this process. Around 0.121 km^2 of the central
640 lobe got detached probably in 2016 associated with the highest mean annual LST
641 recorded since 2002. Modelling results shows (Fig. 11) that the 2016 LST peak
642 propagated down and resulted into increase in thermal regime at 40 m with a lag of
643 four years. Hence, we think both these events are closely linked to the 2016 peak
644 temperature preceded by the warming taking place since 2012. Therefore, this
645 detachment in 2016 was a clear warning sign of the deteriorating health of the
646 cryospheric system which culminated in the present disaster.

647 When recently exposed, bedrock undergoes sudden seasonal temperature variations
648 leading to higher thermal stress, which may increase its susceptibility to rock break
649 down (Wegmann et al., 1998, Fischer et al., 2006., Huggel et al., 2012). Under these
650 facilitating conditions, 2019 experienced the heaviest snowfall in the last 20 years
651 (Mritunjay et al., 2020), which could have accumulated a significant amount of snow
652 over the glacier. Further, heavy snowfall on 4th and 5th February 2021 also added more
653 amount of snow over the glacier. The image just a day before the event shows thick
654 snow accumulation over the glacier, especially above the bergschrund. Such thick
655 snow over the non-glaciated region leads to an eventual warmer ground condition in
656 the winter months compared to snow-free conditions due to the insulation character of
657 the snow. This reflects a lower freezing index of GST during high snow condition as
658 compared to low snow condition (Thayyen et al., under review). Therefore, the
659 seasonal snow accumulation preceding the event might have provided a warmer
660 condition around the frontal margins of the glacier. On the other hand, deeper layers
661 of bedrock up to ~ 40 m were warming as a result of delayed response to LST increase
662 recorded between 2012-2017. Figure 11 shows the lag associated with thermal regime
663 change between the top and bottom layers of the bedrock. The increase of soil
664 temperature of 40-50 m depth initiated in 2012 show highest values in December 2020
665 (probably persisted through February 2021), probably producing conducting warm

666 environment to develop and sustain thin film of water which reduced the bedrock
667 friction. The additional mass from snow accumulation from the latest storm might have
668 provided the final trigger leading to the devastating ice–rock avalanche on 7th February
669 2021. Bringing together all the information generated in the study, we propose the
670 possible geometry and process, which led to the detachment of the right lobe of the
671 hanging glacier (Fig.12). The process is related to glacier headwall erosion and
672 matches closely with the modelling result of glacial erosion focusing on abrasion and
673 plucking (Fig. 12C) (MacGregor et al.,2009). It is to be noted that the spatial and
674 temporal scale of the model varies significantly. However, it gives a good
675 understanding of the processes and highlights the need for such modelling effort in
676 the region for small glaciers. This process of headwall erosion is exacerbated by the
677 recent warming of the ground surface, frost cracking and permafrost thaw and
678 facilitated by increased water availability in the form of increased summer monsoon
679 precipitation and reduction in early winter snow cover. We also propose that the glacier
680 probably gained mass at the accumulation zone owing to the increased summer
681 snowfall. Small glaciers are more susceptible to climate fluctuations and respond
682 faster to the changes. This has been illustrated by recent studies in the region, which
683 suggested small glaciers are losing more mass than big glaciers in recent times
684 (Bhambri et al.,2012; Riyaz et al., 2017; Bankim et al., 2020). This event highlighted
685 the need for improved monitoring of Himalayan cryospheric systems as complex
686 interlinking snow, glacier, permafrost, geology, and climate causes such catastrophic
687 events.

688



689

690

691 Figure 12: Schematic sketch of hanging glacier geometry and possible detachment
 692 process.

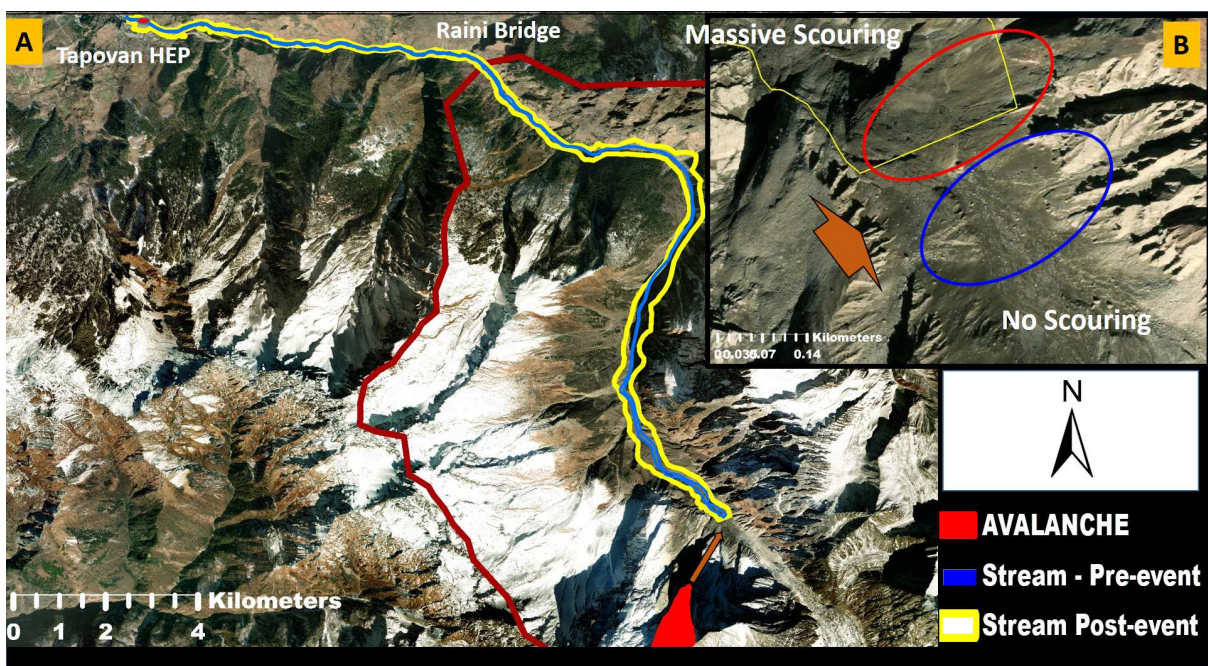
693

694

695 **5.2 Post-event analysis of stream morphology**

696 After the ice-rock avalanche of the Raunthi hanging glacier, it is suggested that the
 697 glacier has melted under frictional heat as it accumulated snow, soil and rocks on its
 698 way downstream and eventually turned into debris flow as it approached the
 699 Rishiganga confluence. Further data and studies are required to rebuild the sequence
 700 of events unfolded and establish its scientific basis. What certain today is the ice
 701 avalanche by a hanging glacier and resultant flood. Snow and soil moisture could add
 702 to the floodwaters. A detailed study is required to see if there was any other source for
 703 flood water. In the absence of clarity on these aspects, we focussed on the analysis of
 704 stream morphological changes between pre-event (used ASTER DEM) and post-
 705 event (used MAXAR) made of high-resolution spectral images. HEC-RAS 5.0.7 was
 706 also used to develop the terrain model of the DEM before generating the stream
 707 geometry, bank lines, and flow paths. The stream length from the strike point to the
 708 bridge is 13.72 km. Due to debris flow from the ice-rock avalanche, a significant
 709 change in the post-event stream width was found. A comparison was made on the

710 surface area of the stream section for the entire length up to the confluence with
 711 Dhauliganga through carefully digitising the pre-event and post-event bank lines. It
 712 was found that the cumulative pre-event stream width for 13.72 km long stretch was
 713 around 50-100 m with a surface area of 0.697 km², whereas the post-event channel
 714 width increased about 200-250 m with about six-folds increase in the stream surface
 715 area (4.22 km²). Figure 13 shows the post-event massive scouring after the initiation
 716 point at Raunthi gad. Figure 13b shows no features indicating flood occurrence from
 717 the Trishul glacier area. However, a detailed field investigation is necessary to confirm
 718 this finding.



719
 720 Figure 13: Images showing a) Pre-event stream width (marked light blue) and Post-
 721 event scouring (Yellow). The location of the hanging glacier and strike point at
 722 Raunthigad (marked red) and the stream reach upstream of strike point (marked blue),
 723 showing no signs of activities ruling out any flood originating upstream of strike point.

724 **5.3 Flood modelling**

725 Developing flood hydrograph originating from such an event is a challenging job. A
 726 number of approximations are required for broad understanding at this early stage.
 727 Here, we used estimated glacier ice volume as the main input. Glacier ice volume
 728 estimated as 11.7 to 13.2 x10⁶ m³. Additionally, snow and soil moisture from the 3.48
 729 km² flood channel area also might have contributed to the final flow volume. As the
 730 flood moved downstream in the Raunthigad, it transformed as debris flow by

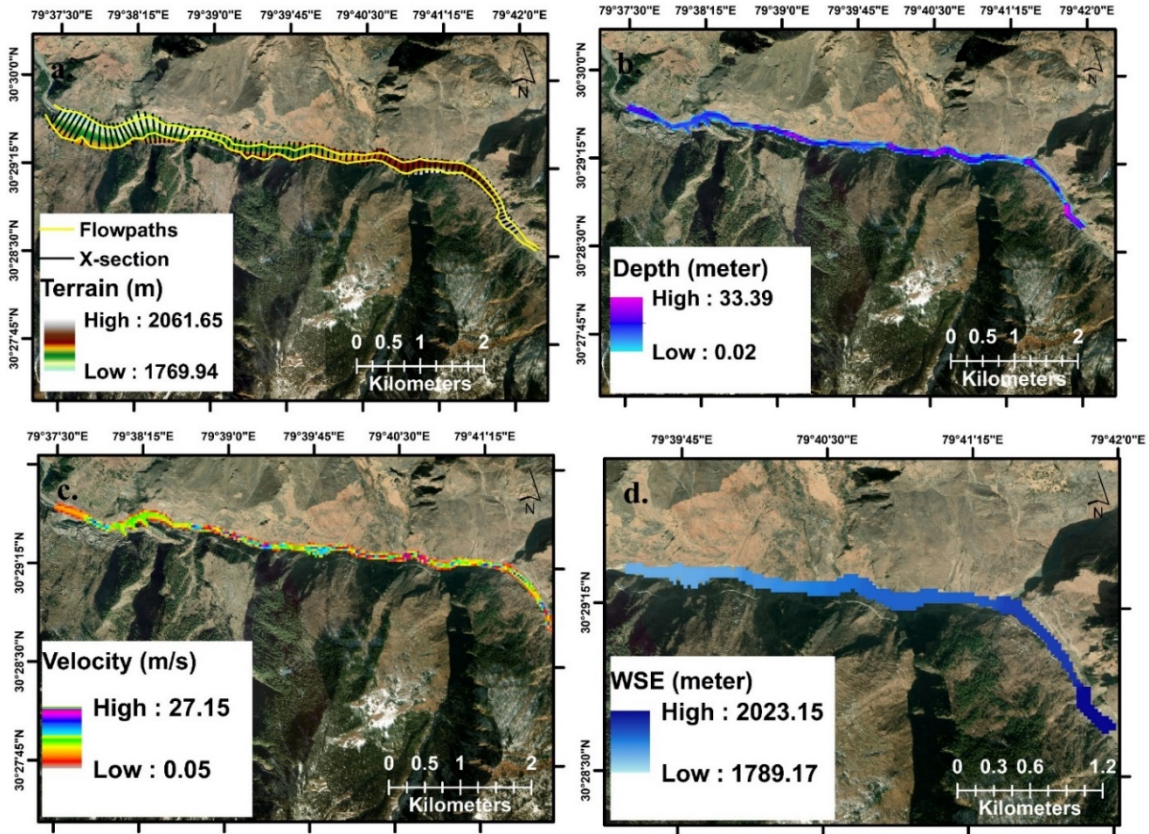
731 incorporating the scoured material along the river reach. Here we are limiting our
732 estimate to a conservative volume of 10 MCM. The generated hydrograph suggested
733 that the peak flow reaches about 5555 m³/s within a period of 20-25 minutes. (Fig. S6).

734 Considering the lack of understanding of the flood generating mechanism at this stage,
735 we consider that the flood acquired its full dimensions about 1 km upstream of the
736 confluence. Taking the generated flood hydrograph as input, we further attempted one-
737 dimensional unsteady flow hydraulic modelling using HEC-RAS 5.0.7 up to the NTPC
738 site located at Tapovan (1800 m a.s.l.). We understand that the flow was
739 supersaturated with debris and ice blocks as learned from local people and could differ
740 with natural streamflow. Specialised debris flow modelling would have been more
741 appropriate under these conditions. The present exercise will provide us with the likely
742 inundation caused due to such a massive flow (~10 MCM), which can be compared
743 with the post-satellite images capturing the inundation.

744 The HEC-RAS model is set up to simulate flow along the part of the Raunthigad,
745 Rishiganga and Dhauliganga. The model result of flow depth, velocity, and maximum
746 water spread elevation is shown in Figure 14. The modelled flood covers the flood
747 channel in a good measure across the channel reach, as seen in the post-event
748 satellite image. The maximum flow depth and velocity simulated utilising the design
749 hydrograph at prominent sections are presented in Table 2. The modelled maximum
750 flow depth and flow velocity reached 33 m and 27 m/s at some cross-sections during
751 simulation, indicating the catastrophic nature of the flood. The flow depth and flow
752 velocity at the bridge location were estimated to be 24 m and 12 m/s, respectively.
753 This bridge is completely washed away during the event. The intensity of flow
754 gradually diminished and reached about 8 m/s at HEP 2 at Tapovan. The estimated
755 flow depth at HEP 2 is 17 m. This analysis provides a first-order estimate of the flood
756 volume without considering entrained debris with the flow. Better dimensions and
757 strength of the debris flow can be modelled separately.

758 Table 2: Maximum flow depth and probable maximum velocity at locations where the
759 flood damaged the structures.

Channel sections	Flow depth (m)	Flow velocity (m/s)
HEP-1	19.7	7.3
BRO Bridge	24.2	12.7
HEP-2	17.7	8.5



760

761 Figure 14: HEC-RAS model set up to simulate flow along the cross-section up to
 762 Tapopan hydropower site

763

764

765

766 **Summary observations**

767 • The event is caused by a complex process involving local geology, snow, glacier,
 768 permafrost processes and recent warming of the local climate.

769 • Regular monitoring of glacier change would have been helped to identify the
 770 earlier advancement and eventual detachment of the central lobe of this hanging
 771 glacier in 2016 and could have served as an early warning.

772 • Such precursors are common in the Alps and other mountain regions, suggesting
 773 an early warning and preparedness is possible in such conditions.

774 • This event highlighted the vulnerability of the Himalayan cryospheric system to
 775 the present warming. System response is building over a period of time due to
 776 increased summer precipitation, elevation-dependent snow cover change,
 777 warming of land surface exacerbated by the seasonal response of reduced snow

778 cover. Delayed response of deeper ground to surface warming, mass balance
779 fluctuations due to increase in summer precipitation etc. This added a new
780 disaster component in the Himalaya, warranting its regular monitoring at least in
781 the area surrounding infrastructure or development projects, including tourism
782 areas.

- 783 • Monitoring the change in precipitation and its form in the high elevation
784 cryospheric areas of the Himalaya is critical for assessing the climate change-
785 related glacier responses. Elevation depended snow cover change produces a
786 warmer environment surrounding the glacier terminus.
- 787 • The response of small glaciers needs regular monitoring as it is more susceptible
788 to changing climate as it respond faster. Also regular monitoring of similar type
789 of glaciers, if any in the region, is required to avoid such type of disasters in
790 future.
- 791 • Permafrost studies, including monitoring of ground surface temperature (GST)
792 and modelling of the ground thermal regime, will provide an early indicator.
793 Permafrost elevations in this area and most of the Indian Himalayan Region is
794 not known, which will further aggravate the risk of the high elevation cryosphere
795 region under a warming climate.

796

797 **Acknowledgements**

798 This work is carried out using the resources from the projects a) National Mission
799 on Sustaining Himalayan Ecosystem (NMSHE), Department of Science and
800 Technology, Ministry of Science and Technology
801 (DST/SPLICE/CCPNMSHE/TF-4/NIH/2015-G) and b) National Mission on
802 Himalayan Studies (NMHS, MoEF&CC) (No. GBPNI/NMHS-2019-20/MG/265).
803 Financial assistance from these projects is highly acknowledged. RJT thank Prof.
804 Stephan Gruber, Carleton University, Canada, for the foresight to install the rock
805 logger in Ladakh and for helping to build permafrost research capability in India.

806 **Funding**

807 This work is carried out using the resources from the projects a) National
808 Mission on Sustaining Himalayan Ecosystem (NMSHE), Department of Science
809 and Technology, Ministry of Science and Technology

810 (DST/SPLICE/CCPNMSHE/TF-4/NIH/2015-G) and b) National Mission on
811 Himalayan Studies (NMHS, MoEF&CC) (No. GBPNI/NMHS-2019-20/MG/265).

812 **Conflicts of interest/Competing interests**

813 The authors have no conflicts of interest to declare that are relevant to the
814 content of this article

815 **Financial interests:** The authors have no relevant financial or non-financial
816 interests to disclose.

817 **Ethical Statement**

818 This material is the authors' own original work, which has not been previously
819 published elsewhere. The paper is not currently being considered for publication
820 elsewhere. The paper reflects the authors' own research and analysis in a truthful
821 and complete manner. Sources all information used in the MS are properly
822 disclosed.
823

824 **Availability of data and material**

825 Not applicable.

826 **Code availability**

827 Not applicable.

828

829 **Authors' contributions**

830 Renoj Thayyen conceived the study, contributed to the data analysis and wrote
831 the first draft of the paper. P.K. Mishra and Hemant Singh carried out the flood
832 modelling and remote sensing data analysis. Sanjay Jain contributed to study
833 conceptualization and editing. John Wani run the GEOtop model and permafrost
834 analysis. Mrintujay K. Singh carried out snow cover estimation and Bankim
835 Yadav worked on GPM and LST data. All the authors contributed to paper writing
836 and editing.

837 **References**

838 Allen, S. K., Rastner, P., Arora, M., Huggel, C., & Stoffel, M. (2016). Lake outburst and
839 debris flow disaster at Kedarnath, June 2013: hydrometeorological triggering and
840 topographic predisposition. *Landslides*, 13(6), 1479-1491.

841 Alley, R. B., Strasser, J. C., Lawson, D. E., Evenson, E. B., & Larson, G. J. (1999).
842 Glaciological and geological implications of basal-ice accretion in
843 overdeepenings. *Special Paper of the Geological Society of America*, 337, 1-9.

- 844 Bahr, D. B., Meier, M. F., & Peckham, S. D. (1997). The physical basis of glacier
845 volume-area scaling. *Journal of Geophysical Research: Solid Earth*, 102(B9),
846 20355-20362.
- 847 Bhambri, R., Bolch, T., & Chaujar, R. K. (2012). Frontal recession of Gangotri Glacier,
848 Garhwal Himalayas, from 1965 to 2006, measured through high-resolution remote
849 sensing data. *Current Science*, 102(3), 489-494.
- 850 Bhandary, N. P., Dahal, R. K., & Okamura, M. (2012). Preliminary understanding of
851 the Seti River debris-flood in Pokhara, Nepal, on May 5th, 2012-A report based on
852 a quick field visit program. *ISSMGE Bulletin*, 6(4), 8-18.
- 853 Bookhagen, B., & Burbank, D. W. (2006). Topography, relief, and TRMM-derived
854 rainfall variations along the Himalaya. *Geophysical Research Letters*, 33(8).
- 855 Bookhagen, B., & Burbank, D. W. (2010). Toward a complete Himalayan hydrological
856 budget: Spatiotemporal distribution of snowmelt and rainfall and their impact on
857 river discharge. *Journal of Geophysical Research: Earth Surface*, 115(F3).
- 858 Changwei, X., Gough, W. A., Lin, Z., Tonghua, W., & Wenhui, L. (2015). Temperature-
859 dependent adjustments of the permafrost thermal profiles on the Qinghai-Tibet
860 Plateau, China. *Arctic, Antarctic, and Alpine Research*, 47(4), 719-728.
- 861 Cheng, G., & Wu, T. (2007). Responses of permafrost to climate change and their
862 environmental significance, Qinghai-Tibet Plateau. *Journal of Geophysical
863 Research: Earth Surface*, 112(F2).
- 864 Das, S., Ashrit, R., & Moncrieff, M. W. (2006). Simulation of a Himalayan cloudburst
865 event. *Journal of earth system science*, 115(3), 299-313.
- 866 Dimri, A. P., Chevuturi, A., Niyogi, D., Thayyen, R. J., Ray, K., Tripathi, S. N., Pandey,
867 A. K. Mohanty, U. C. (2017). Cloudbursts in Indian Himalayas: a review. *Earth-
868 Science Reviews*, 168, 1-23.
- 869 Dobhal, D. P., Mehta, M., & Srivastava, D. (2013). Influence of debris cover on
870 terminus retreat and mass changes of Chorabari Glacier, Garhwal region, central
871 Himalaya, India. *Journal of Glaciology*, 59(217), 961-971.
- 872 Dubey, C. S., Shukla, D. P., Ningreichon, A. S., & Usham, A. L. (2013). Orographic
873 control of the Kedarnath disaster. *Current Science*, 105(11), 1474-1476.
- 874 Dwivedi, S., & Neupane, Y. (2013). Cause and mechanism of the Seti River flood, 5th
875 May 2012, western Nepal. *Journal of Nepal Geological Society*, 46, 11-18.
- 876 Endrizzi, S., Gruber, S., Dall'Amico, M., & Rigon, R. (2014). GEOtop 2.0: simulating
877 the combined energy and water balance at and below the land surface accounting
878 for soil freezing, snow cover and terrain effects. *Geoscientific Model
879 Development*, 7(6), 2831-2857.
- 880 Evans, S. G., & Delaney, K. B. (2015). Catastrophic mass flows in the mountain glacial
881 environment. In *Snow and ice-related hazards, risks and disasters* (pp. 563-606).
882 Academic Press.
- 883 Evans, S. G., & Ge, S. (2017). Contrasting hydrogeologic responses to warming in
884 permafrost and seasonally frozen ground hillslopes. *Geophysical Research
885 Letters*, 44(4), 1803-1813.

- 886 Evans, S. G., Tutubalina, O. V., Drobyshev, V. N., Chernomorets, S. S., McDougall,
887 S., Petrakov, D. A., & Hungr, O. (2009). Catastrophic detachment and high-velocity
888 long-runout flow of Kolka Glacier, Caucasus Mountains, Russia in
889 2002. *Geomorphology*, 105(3-4), 314-321.
- 890 Fischer, L., Käab, A., Huggel, C., & Noetzi, J. (2006). Geology, glacier retreat and
891 permafrost degradation as controlling factors of slope instabilities in a high-
892 mountain rock wall: the Monte Rosa east face. *Natural Hazards and Earth System
893 Sciences*, 6(5), 761-772.
- 894 Gubler, S., Endrizzi, S., Gruber, S., & Purves, R. S. (2013). Sensitivities and
895 uncertainties of modeled ground temperatures in mountain
896 environments. *Geoscientific Model Development*, 6(4), 1319-1336.
- 897 Haeberli, W., Huggel, C., Käab, A., Zraggen-Oswald, S., Polkvoj, A., Galushkin, I.,
898 Zotikov, I & Osokin, N. (2004). The Kolka-Karmadon rock/ice slide of 20
899 September 2002: an extraordinary event of historical dimensions in North Ossetia,
900 Russian Caucasus. *Journal of Glaciology*, 50(171), 533-546
- 901 Hanisch, J., Koirala, A., & Bhandary, N. P. (2013). The Pokhara May 5th flood disaster:
902 a last warning sign sent by nature?. *Journal of Nepal Geological Society*, 46, 1-10.
- 903 Hooke, R. L. (1991). Positive feedbacks associated with erosion of glacial cirques and
904 overdeepenings. *Geological Society of America Bulletin*, 103(8), 1104-1108.
- 905 Huffman, G. J., Bolvin, D. T., Braithwaite, D., Hsu, K. L., Joyce, R. J., Kidd, C., Eric J.
906 Nelkin & Xie, P. (2020). Integrated multi-satellite retrievals for the Global
907 Precipitation Measurement (GPM) Mission (IMERG). In *Satellite precipitation
908 measurement* (pp. 343-353). Springer, Cham.
- 909 Huggel, C., Allen, S., Deline, P., Fischer, L., Noetzi, J., & Ravanel, L. (2012). Ice
910 thawing, mountains falling—are alpine rock slope failures increasing?. *Geology
911 Today*, 28(3), 98-104.
- 912 Huggel, C., Zraggen-Oswald, S., Haeberli, W., Käab, A., Polkvoj, A., Galushkin, I., &
913 Evans, S. G. (2005). The 2002 rock/ice avalanche at Kolka/Karmadon, Russian
914 Caucasus: assessment of extraordinary avalanche formation and mobility, and
915 application of QuickBird satellite imagery. *Natural Hazards and Earth System
916 Sciences*, 5(2), 173-187.
- 917 Jeng, R. I. (2006). NRCS (SCS) synthetic curvilinear dimensionless unit
918 hydrograph. *Journal of irrigation and drainage engineering*, 132(6), 627-631.
- 919 Kargel, J., Leonard, G., Paudel, L., Regmi, D., Bajracharya, S., Fort, M., Joshi, S.,
920 Poudel, K., Thapa, B. & Watanabe, T. (2014). The 2012 Seti River flood disaster
921 and alpine cryospheric hazards facing Pokhara, Nepal. In EGU General Assembly
922 Conference Abstracts (p. 12448).
- 923 Kim, D. E., Seong, Y. B., Choi, K. H., & Yu, B. Y. (2017). Role of debris flow on the
924 change of ¹⁰Be concentration in rapidly eroding watersheds: a case study on the
925 Seti River, central Nepal. *Journal of Mountain Science*, 14(4), 716-730.
- 926 Komori, J., Koike, T., Yamanokuchi, T., & Tshering, P. (2012). Glacial lake outburst
927 events in the Bhutan Himalayas. *Global Environmental Research*, 16(February
928 2012), 59-70.

- 929 Kumar, A., Gupta, A. K., Bhambri, R., Verma, A., Tiwari, S. K., & Asthana, A. K. L.
930 (2018). Assessment and review of hydrometeorological aspects for cloudburst and
931 flash flood events in the third pole region (Indian Himalaya). *Polar Science*, 18, 5-
932 20.
- 933 MacGregor, K. R., Anderson, R. S., & Waddington, E. D. (2009). Numerical modeling
934 of glacial erosion and headwall processes in alpine
935 valleys. *Geomorphology*, 103(2), 189-204.
- 936 MacGregor, K. R., Anderson, R. S., & Waddington, E. D. (2009). Numerical modeling
937 of glacial erosion and headwall processes in alpine
938 valleys. *Geomorphology*, 103(2), 189-204.
- 939 Mergili, M., Emmer, A., Juřicová, A., Cochachin, A., Fischer, J. T., Huggel, C., &
940 Pudasaini, S. P. (2018). How well can we simulate complex hydro-geomorphic
941 process chains? The 2012 multi-lake outburst flood in the Santa Cruz Valley
942 (Cordillera Blanca, Perú). *Earth surface processes and landforms*, 43(7), 1373-
943 1389.
- 944 Mergili, M., Jaboyedoff, M., Pullarello, J., & Pudasaini, S. P. (2020). Back calculation
945 of the 2017 Piz Cengalo–Bondo landslide cascade with r. avaflow: what we can
946 do and what we can learn. *Natural Hazards and Earth System Sciences*, 20(2),
947 505-520.
- 948 Ol, H., Higaki, D., Yagi, H., Usuki, N., & Yoshino, K. (2014). Report of the investigation
949 of the flood disaster that occurred on May 5, 2012 along the Seti River in
950 Nepal. *International Journal of Erosion Control Engineering*, 7(4), 111-117.
- 951 Paterson, W. S. B. (1994). *Physics of glaciers*. Butterworth-Heinemann.
- 952 Pogliotti, P., 2011. Influence of snow cover on MAGST over complex morphologies in
953 mountain permafrost regions. University of Torino, Torino.
- 954 Preh, A., & Sausgruber, J. T. (2015). The extraordinary rock-snow avalanche of Alpl,
955 Tyrol, Austria. Is it possible to predict the runout by means of single-phase
956 Voellmy-or Coulomb-type models?. In *Engineering Geology for Society and*
957 *Territory-Volume 2* (pp. 1907-1911). Springer, Cham.
- 958 Raj, K. G., & Kumar, K. V. (2012). Assessment of supraglacial lake growth from multi-
959 temporal satellite data—a case study of Vasundhara Tal, Kumaun Himalaya,
960 India. *Himalayan Geology*, 33(1), 53-58.
- 961 Riyaz Ahmad Mir, Sanjay K. Jain, Sharad K. Jain, Thayyen, R.J, Arun K. Saraf (2017):
962 Assessment of recent glacier changes and its controlling factors from 1976 to 2011
963 in Baspa basin, western Himalaya, Arctic, Antarctic, and Alpine Research DOI:
964 <http://dx.doi.org/10.1657/AAAR0015-070>.
- 965 Röthlisberger, H. (1987). Sliding phenomena in a steep section of Balmhorngletscher,
966 Switzerland. *Journal of Geophysical Research: Solid Earth*, 92(B9), 8999-9014.
- 967 Sangewar, C. V., & Shukla, S. P. (2009). Inventory of the Himalayan glaciers: a
968 contribution to the international hydrological programme. Geological Survey of
969 India, Special publication number 34.
- 970 Savi, S., Comiti, F., & Strecker, M. R. (2021). Pronounced increase in slope instability
971 linked to global warming: a case study from the Eastern European Alps. *Earth*
972 *Surface Processes and Landforms*.

- 973 Schmidt, S., Nüsser, M., Baghel, R., & Dame, J. (2020). Cryosphere hazards in
974 Ladakh: the 2014 Gya glacial lake outburst flood and its implications for risk
975 assessment. *Natural Hazards*, 104(3), 2071-2095.
- 976 Singh, M. K., Thayyen, R. J., & Jain, S. K. (2019). Snow cover change assessment in
977 the upper Bhagirathi basin using an enhanced cloud removal algorithm. *Geocarto*
978 *International*, 1-24.
- 979 Soil Conservation Service (SCS). (1964). National engineering handbook, Sec. 4, U.S.
980 Dept. of Agriculture, Washington, D.C.
- 981 Thayyen, R. J. (2020). Hydrology of the Cold-Arid Himalaya. In *Himalayan Weather*
982 *and Climate and their Impact on the Environment* (pp. 399-417). Springer, Cham.
- 983 Thayyen, R. J., & Dimri, A. P. (2018). Slope environmental lapse rate (SELR) of
984 temperature in the monsoon regime of the western Himalaya. *Frontiers in*
985 *Environmental Science*, 6, 42.
- 986 Thayyen, R. J., Dimri, A. P., Kumar, P., & Agnihotri, G. (2013). Study of cloudburst and
987 flash floods around Leh, India, during August 4–6, 2010. *Natural hazards*, 65(3),
988 2175-2204.
- 989 Thayyen, R. J., Gergan, J. T., & Dobhal, D. P. (2005). Slope lapse rates of temperature
990 in Din Gad (Dokriani glacier) catchment, Garhwal Himalaya, India. *Bulletin of*
991 *Glaciological Research*, 22, 31-37.
- 992 Thayyen, R.J., Wani, J. M., and Gruber, S. Permafrost in the Upper Indus Basin: A
993 case study of active layer dynamics and hydrology in cold-arid Ladakh (Under
994 Review)
- 995 Thayyen, R.J., Goel, M. K., and Kumar, N. (2010). Estimation of aerial and volumetric
996 changes for selected glaciers in Jammu & Kashmir. Project report, National
997 Institute of Hydrology, WHRC, Jammu, 1-92.
- 998 Wani, J. M., Thayyen, R. J., Gruber, S., Ojha, C. S. P., & Stumm, D. (2020). Single-
999 year thermal regime and inferred permafrost occurrence in the upper Ganglass
1000 catchment of the cold-arid Himalaya, Ladakh, India. *Science of the Total*
1001 *Environment*, 703, 134631.
- 1002 Wegmann, M., Gudmundsson, G. H., & Haeberli, W. (1998). Permafrost changes in
1003 rock walls and the retreat of Alpine glaciers: a thermal modelling
1004 approach. *Permafrost and Periglacial Processes*, 9(1), 23-33.
- 1005 Wu, Q., & Zhang, T. (2008). Recent permafrost warming on the Qinghai-Tibetan
1006 Plateau. *Journal of Geophysical Research: Atmospheres*, 113(D13).
- 1007 Wu, Q., Zhang, T., & Liu, Y. (2010). Permafrost temperatures and thickness on the
1008 Qinghai-Tibet Plateau. *Global and Planetary Change*, 72(1-2), 32-38.
- 1009 Yadav, B. C., Thayyen, R. J., & Jain, K. (2020). Topoclimatic zones and characteristics
1010 of the upper Ganga basin, Uttarakhand, India. *International Journal of*
1011 *Climatology*, 40(14), 6002-6019.
- 1012
- 1013

Figures



Figure 1

a) Pre-flood NTPC barrage (HEP 2) at Tapovan, b) Post flood photo showing severe damage to NTPC barrage at Tapovan C) Site of washed off bridge across Rishiganga upstream of NTPC barrage D) Site of Rishiganga (HEP-1) project site Photo courtesy: NTPC and BRO

Drainage map

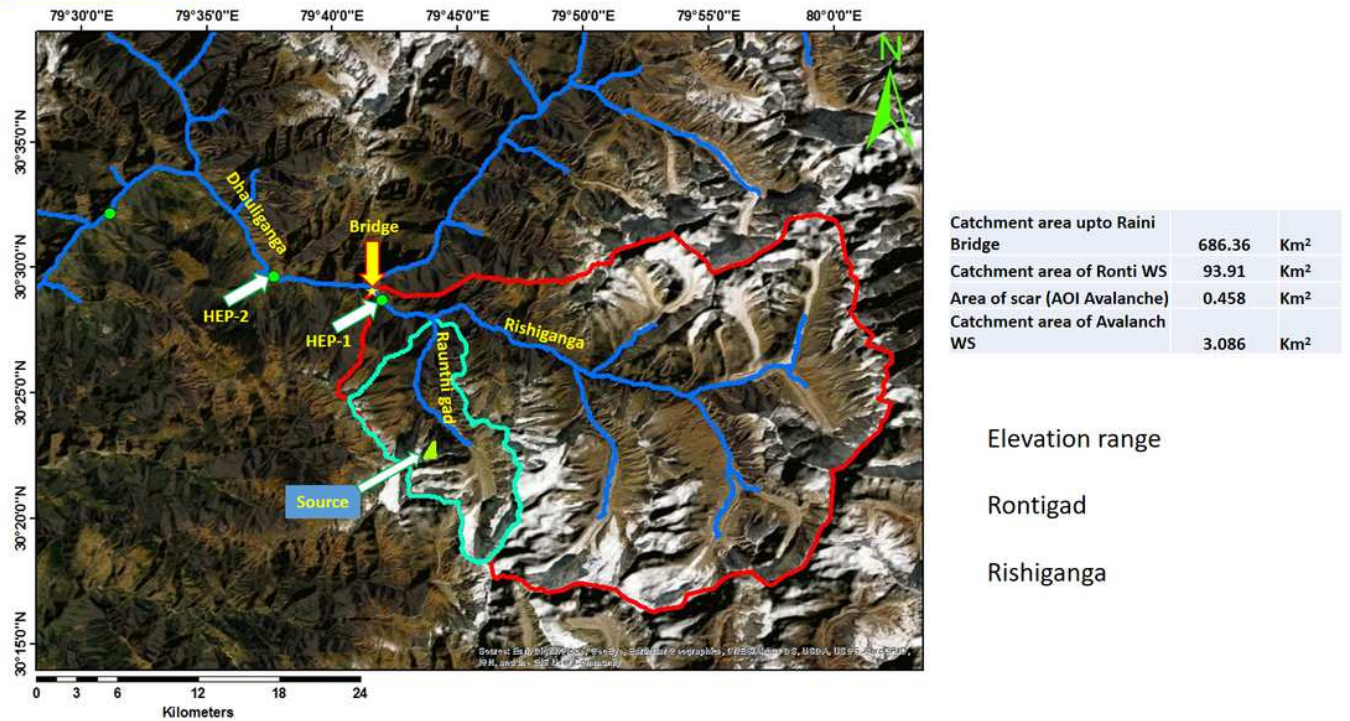


Figure 2

The drainage map of the area showing the Raunthigad catchment and potential source area of the ice-rock avalanche, Rishiganga catchment and Dhauliganga and Alakananda rivers further downstream.

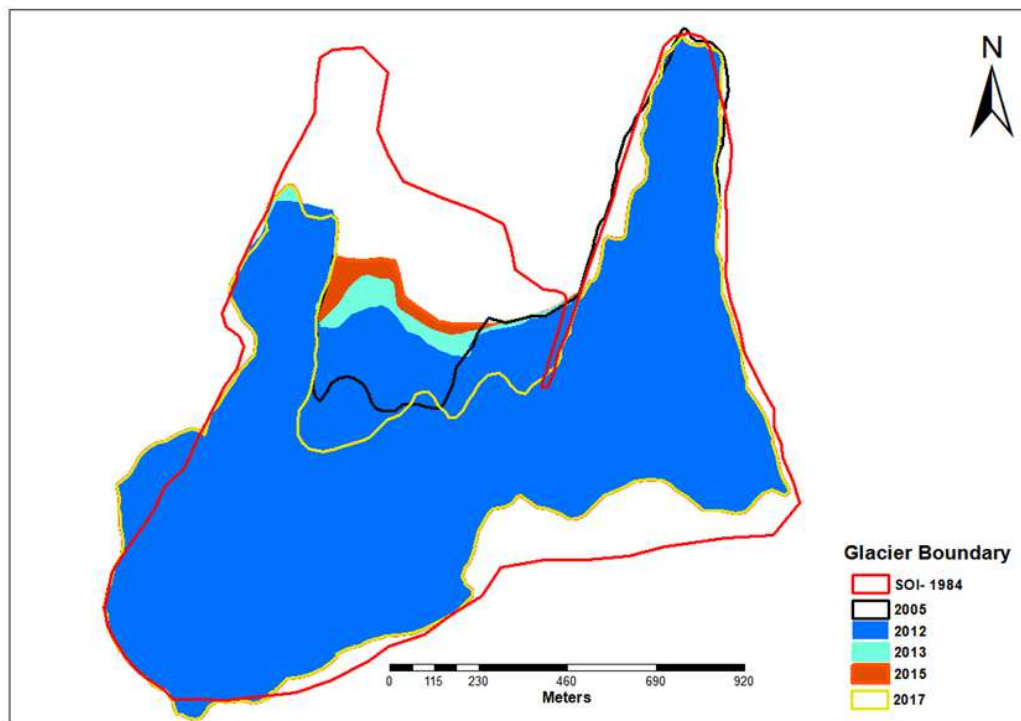


Figure 3

Glacier area change since 1984 showing steady-state conditions of right detached lobe for 33 years and significant area change for left central lobes

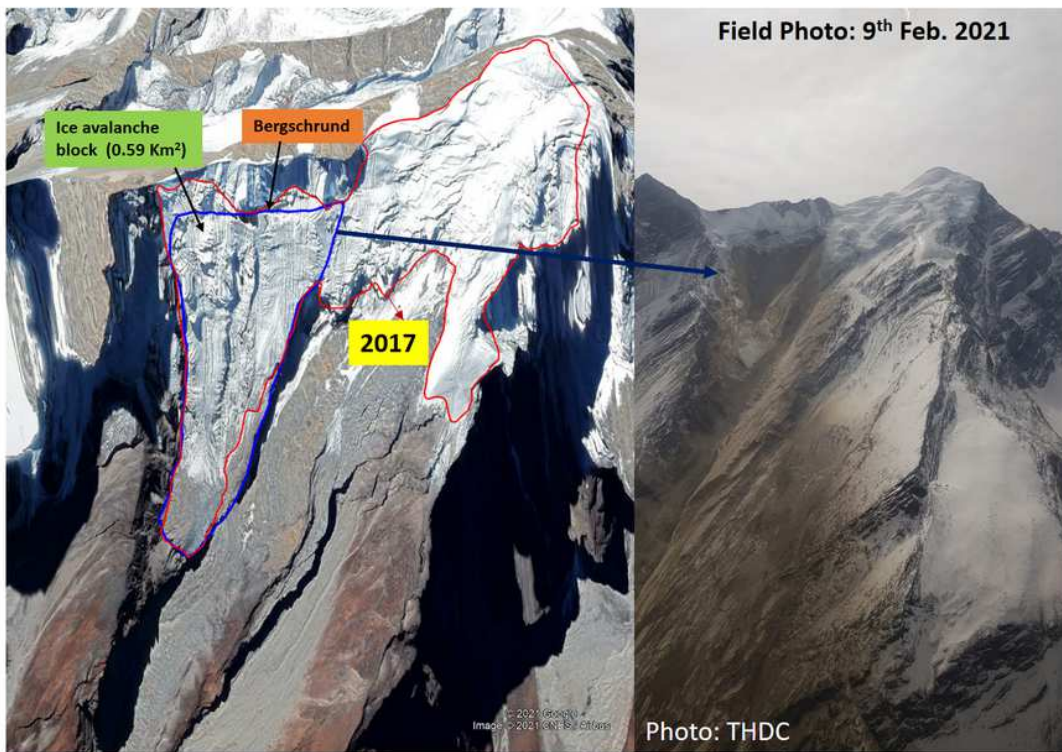


Figure 4

A) Hanging glacier in google earth image of 2017. The detached right lobe is marked blue. B) Heli photo of 9th February 2021 of the site showing detachment of the glacier creating an ice-rock avalanche. (Photo courtesy, THDC)

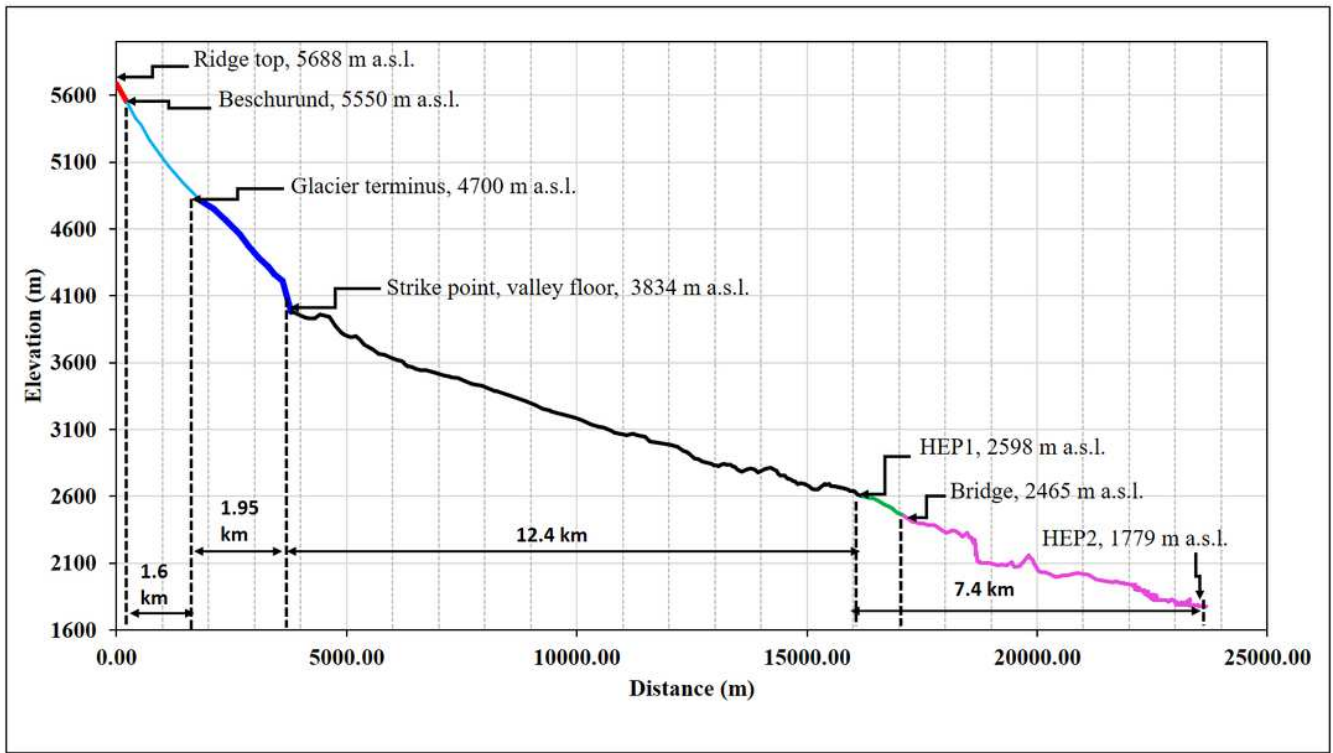


Figure 5

Elevation profile for the stretch between ridge top to HEP 2 at Tapovan.

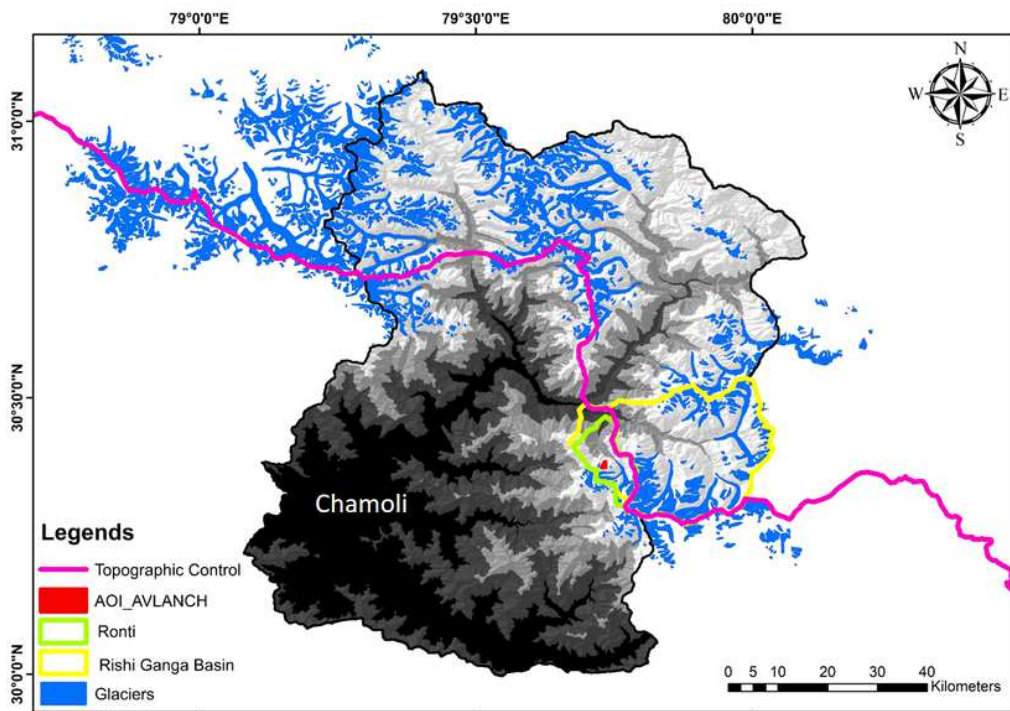


Figure 6

Topography control (TC) dividing the monsoon and monsoon deficit zone in Uttarakhand. Note the location of the Raunthigad catchment and the location of the avalanche zone southern side close to the TC. (Modified after Bankim et al., 2020)

Precipitation change

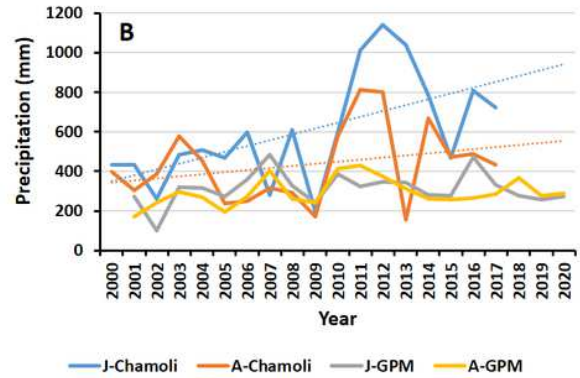
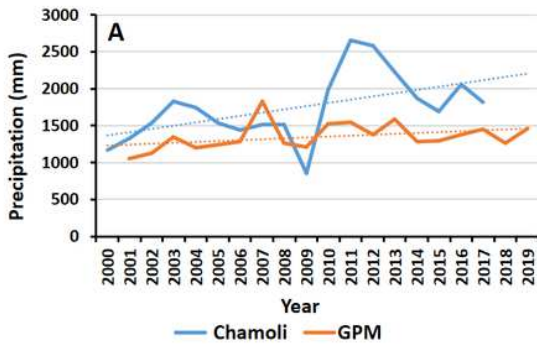


Figure 7

Precipitation over the region showing an increasing trend for the station and GPM data A) Annual precipitation B) July and August precipitation.

Snow cover change

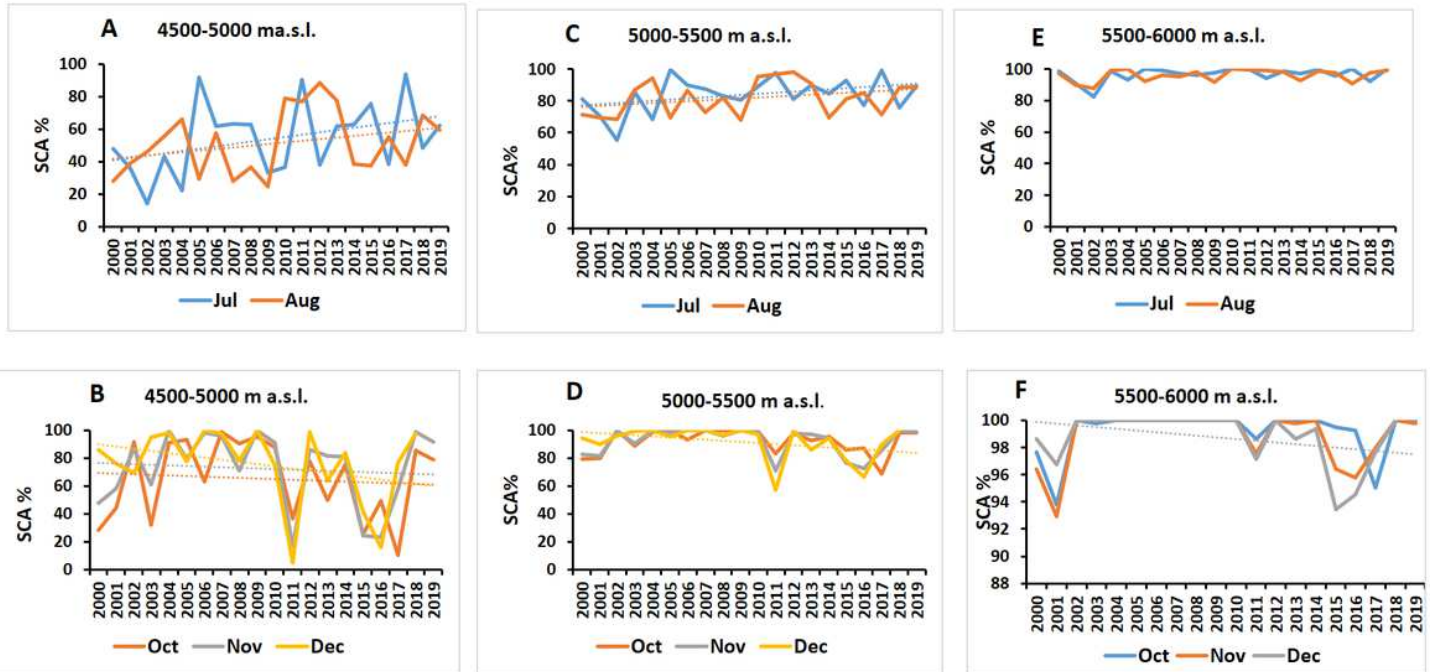


Figure 8

Elevation-depended seasonal change in snow cover in the glacier elevations of Raunthi gad showing an increasing trend in monsoon months and decreasing trend in October, November and December months. Decreasing trend is significant since 2010.

LST change

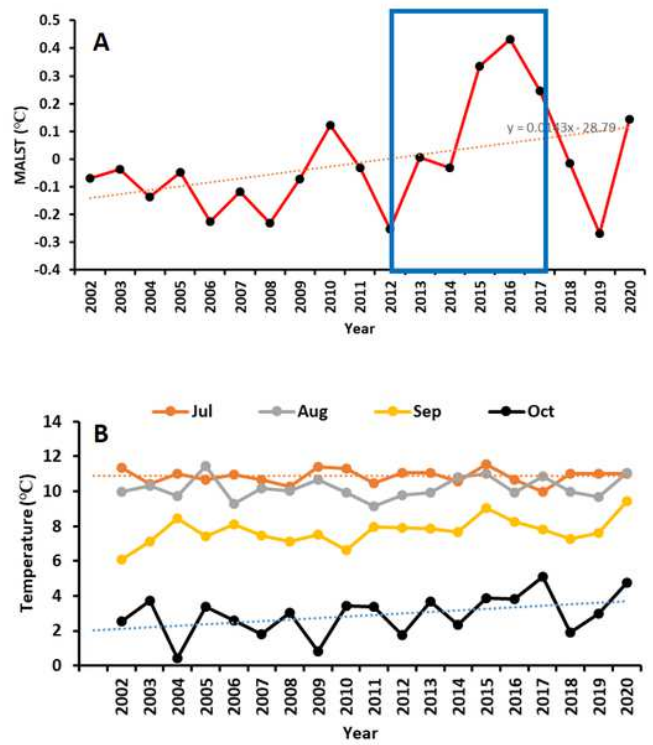
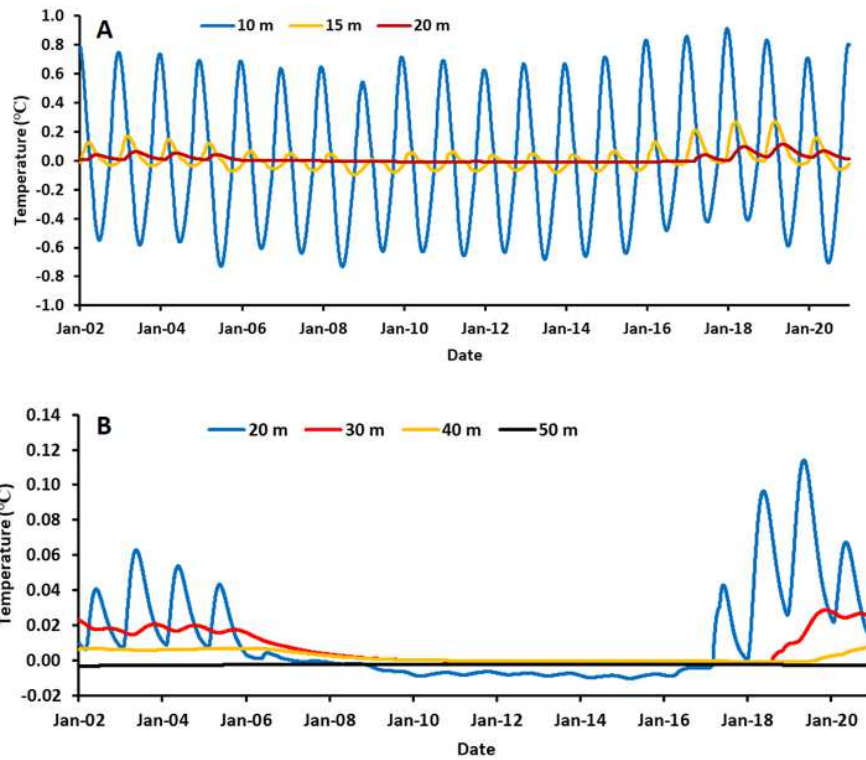


Figure 9

a) Mean Annual LST variation around hanging glacier area during 2002-2020 b) LST variation during July, August, September and October showing a significant rise from 2012 to 2016 also reflected in October LST. Peak monsoon months show no increase in LST.



Soil Temperature at Rishi Ganga Slide site with modelled GST as input for high diffusivity case

Figure 10

a) Modelled monthly mean temperature variation at a) 10,15 and 20 m and b) 20, 30, 40 and 50 m showing the seasonal changes and delayed warming towards deeper depths

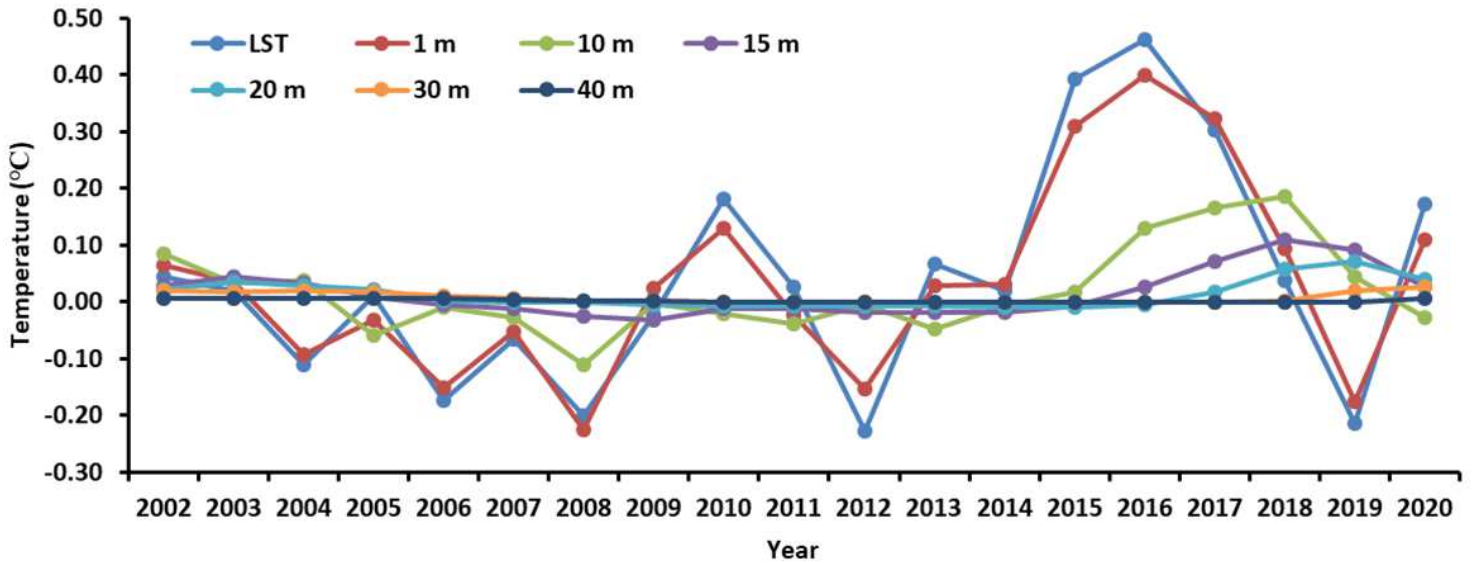


Figure 11

Delayed response of deeper depth to LST increase from 2012, which peaked in 2016. A 4year delay at 40 m forced the highest temperature between 40-50 m during December-February.

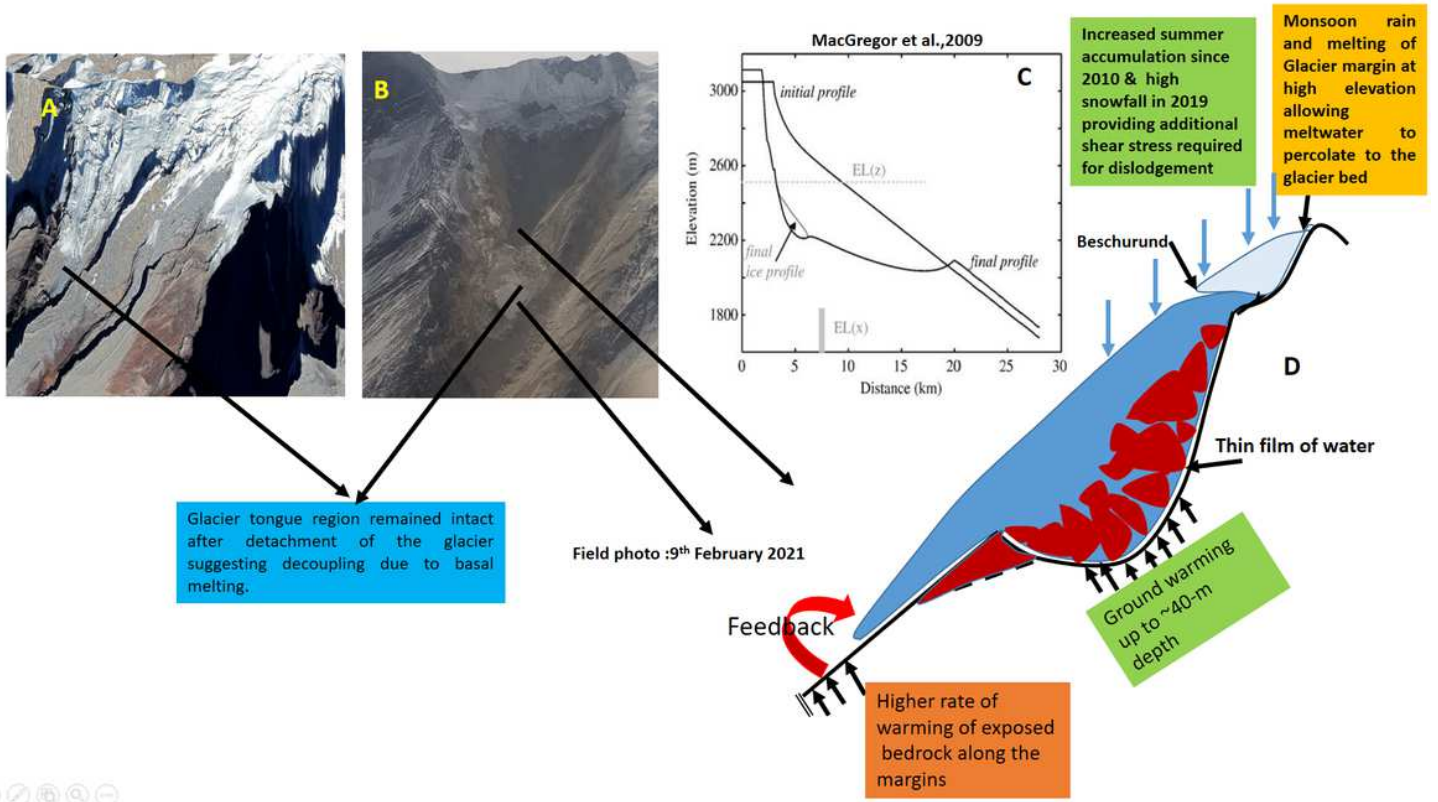


Figure 12

Schematic sketch of hanging glacier geometry and possible detachment process.

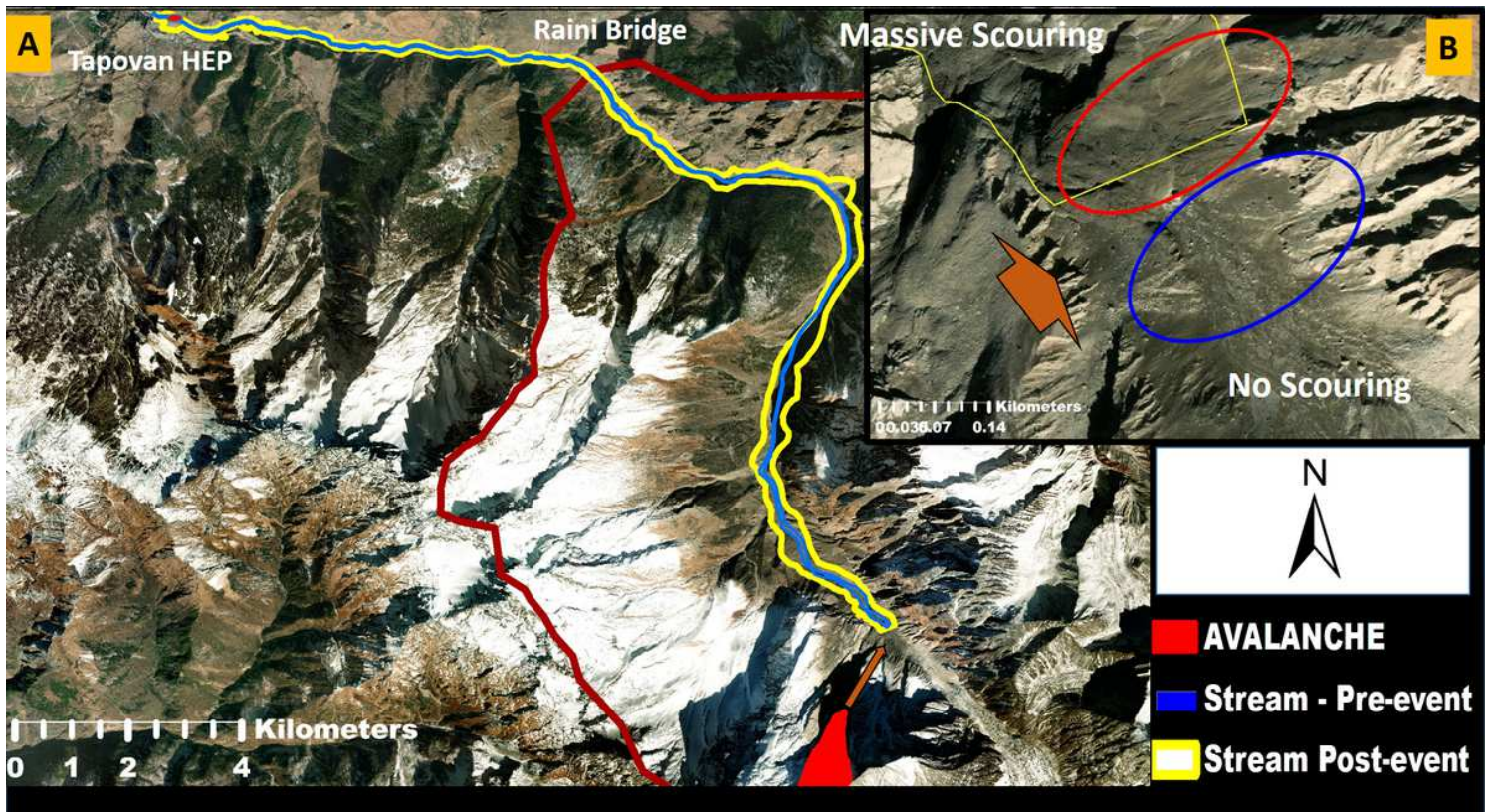


Figure 13

Images showing a) Pre-event stream width (marked light blue) and Post-event scouring (Yellow). The location of the hanging glacier and strike point at Raunthigad (marked red) and the stream reach upstream of strike point (marked blue), showing no signs of activities ruling out any flood originating upstream of strike point.

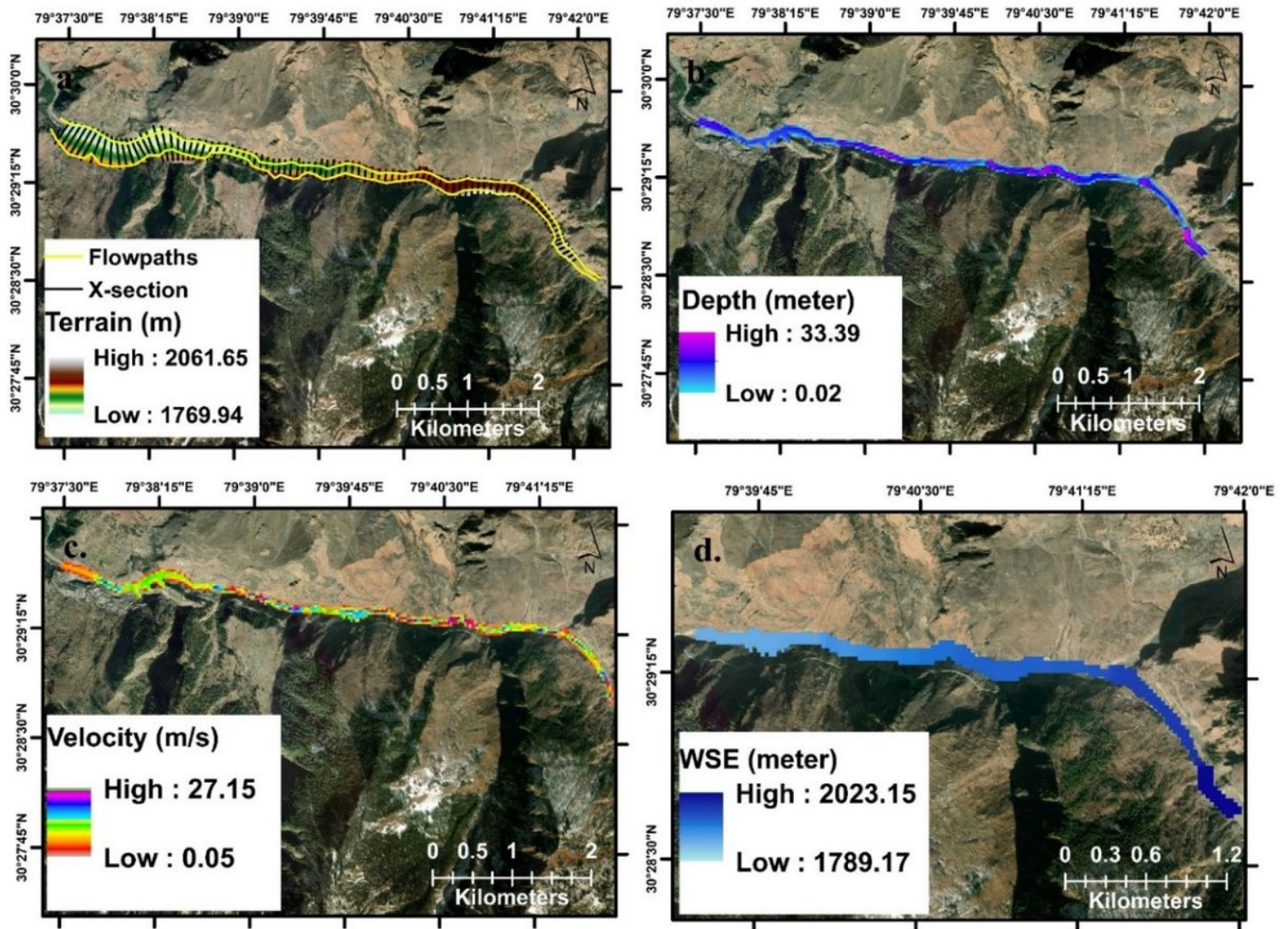


Figure 14

HEC-RAS model set up to simulate flow along the cross-section up to Tapopan hydropower site

Supplementary Files

This is a list of supplementary files associated with this preprint. Click to download.

- [RishiSupplementary16March.docx](#)